Retrieval of wind, temperature, water vapor and other trace constituents in the Martian Atmosphere

William G. Read, Leslie K. Tamppari, Nathaniel J. Livesey, R. Todd Clancy, François Forget, Paul Hartogh, Scot C. R. Rafkin, Goutam Chattopadhyay

Retrieval of wind, temperature, water vapor and other trace constituents in the Martian Atmosphere.

William G. Read[a,*], Leslie K. Tamppari[a], Nathaniel J. Livesey[a], R. Todd Clancy[b], François Forget[c], Paul Hartogh[d], Scot C. R. Rafkin[e], Goutam Chattopadhyay[a]

[a]*Jet Propulsion Laboratory/California Institute of Technology, 4800 Oak Grove Drive, Pasadena, California, 91109*
[b]*Space Science Institute, POB 3075, Bald Head Isl, NC 28461 USA*
[c]*Laboratoire de Météorologie Dynamique, CNRS, Paris, France*
[d]*Max-Planck-Institut für Sonnensystemforschung, Justus von Liebig Weg 3, D-37077 Gottingen, Germany*
[e]*Southwest Research Institude, 1050 Walnut St, Suite 300, Boulder, CO 80302 USA*

Abstract

Atmospheric limb sounding is a well-established technique for measuring atmospheric temperature, composition, and wind. The theoretical capabilities of a submillimeter limb sounder placed in low Mars orbit are quantified, with a particular focus on the ability to make profile measurements of line-of-sight wind, temperature, water vapor, deuterated water vapor, several isotopes of carbon monoxide, oxygen-18 carbon dioxide, ozone, and hydrogen peroxide. We identify cases where all such measurements can be made within a single 25–70 GHz wide region of the submillimeter spectrum, enabling use of a single state-of-the-art submillimeter receiver. Six potential spectral regions, approximately centered at 335 GHz, 450 GHz, 550 GHz, 900 GHz, 1000 GHz, and 1130 GHz are found, any one of which can provide a complete measurement suite. The expected precision and vertical resolution of temperature, composition, and wind measurements from instruments in each range are quantified. This work thus follows on from that of Urban et al. (2005), Kasai et al. (2012), and earlier studies, expanding them to consider many alternative observing frequency regions. In general, performance (in terms of measurement precision and vertical resolution) is improved with increasing observation frequency. In part this is due to our choice to assume the same antenna size for each frequency, thus providing a narrower field of view for the higher frequency configurations. The general increase in emission line strengths with increasing frequency also contributes to this improved performance in some cases. However, increased instrument power needs for the higher frequency configurations may argue against their choice in some mission scenarios.

Keywords: Mars, Atmosphere, Wind, isotopes, temperature, humidity, composition

*Corresponding author

Email addresses: william.g.read@jpl.nasa.gov (William G. Read), leslie.k.tamppari@jpl.nasa.gov (Leslie K. Tamppari), nathaniel.j.livesey@jpl.nasa.gov (Nathaniel J. Livesey), clancy@spacescience.org (R. Todd Clancy), francois.forget@lmd.jussieu.fr (François Forget), hartogh@mps.mpg.de (Paul Hartogh), rafkin.swri@gmail.com (Scot C. R. Rafkin), Goutam.Chattopadhyay@jpl.nasa.gov (Goutam Chattopadhyay)

1. Introduction

The study of the Martian atmosphere and climate commenced in the early days of telescopic observations of Mars and continues through today. Much has been learned, especially over the last several decades, thanks to a spaceborne observing program including both orbiters and landed assets. We now have long-duration, global-scale aerosol column and profile measurements, temperature profile measurements, aerosol and cloud imagery, daytime water vapor column, and measurements of some trace gases such as ozone, oxygen, and H_2O_2 (e.g., Smith et al., 2001, 2009; Malin et al., 2008; Kleinböhl et al., 2009; Clancy et al., 2016; Montmessin et al., 2017; Hartogh et al., 2010b; Encrenaz et al., 2012, 2015). Additionally, the ExoMars Trace Gas Orbiter (Korablev et al., 2014; Robert et al., 2016) will measure profiles of the abundance of many key trace gases at certain locations via solar occultation, and the Mars Atmosphere and Evolution Mission (MAVEN, Jakosky et al., 2015) is studying ozone, and the upper atmosphere and its interaction with the space environment. While existing and upcoming datasets are rich and our understanding of the Martian weather and climate has improved greatly in recent years, direct measurements of winds and vertical profiles of water vapor are key outstanding measurement needs.

The winds on Mars are almost completely unknown, yet are critical for understanding fundamental Martian processes driving the dust and water cycles, and for ensuring safe landing of robotic and human spacecraft. Previous Martian surface wind measurements are limited to the Viking, Pathfinder, Phoenix and Curiosity landed missions; all single locations with only the Vikings operating contemporaneously. A few other indirect wind measurements have been made through the examination of wind generated features on the surface (e.g., Greeley et al., 1993), cloud motions (Kahn, 1983; Zurek et al., 1992), and spacecraft aerobraking (Baird et al., 2007; Crowley and Tolson, 2007). A few Earth-based observations of the Doppler shift of atmospheric spectral lines have allowed wind retrievals (Sonnabend et al., 2012, 2006; Moreno et al., 2009), but they are severely limited in time and represent averages over very large regions of the atmosphere (Kuroda and Hartogh, 2010). Large-scale winds have also been diagnosed indirectly from vertical temperature soundings via quasi-geostrophic thermal wind balance (e.g., Smith et al., 2001). However, this approximation is likely to be significantly in error on Mars due to substantial ageostrophic flows and strong waves that may even result in mechanically forced wind reversals (Medvedev et al., 2011b). Moreover, thermal infrared temperature retrievals can be affected by large amounts of aerosols (e.g., a very cloudy environment; D. Kass, pers. comm., 2017).

The Martian water vapor cycle, one of three main cycles operating on Mars today, supports both the dominant catalytic cycles driving Mars atmospheric chemistry (e.g., Nair et al., 1994) and the formation of Mars water-ice clouds, which influence dust aerosols as well as global transport through microphysical and radiative heating effects (e.g., Madeleine et al., 2012). Despite the importance of water in the Mars climate and atmosphere, there exists only limited sampling of Mars atmospheric water vapor as a function of altitude. Mars Express solar occultation profile determinations (Fedorova et al., 2009; Maltagliati et al., 2011, 2013) are very limited in spatial and seasonal coverage, and exhibit extreme variability in the altitude behavior of water abundances over ~25–60 km. Despite the limited nature of these measurements, analyzing them in the context of contemporaneous temperature measurements suggests surprisingly large supersaturation conditions with respect to water ice cloud formation (Maltagliati et al., 2011). More extensive seasonal and spatial distributions for vertical water vapor profiles have been inferred from Mars Reconnaissance Orbiter limb profile retrievals for near-IR O_2 airglow, which is inversely proportional to water vapor (Clancy et al., 2017). These coarse seasonal/spatial characterizations of the global distribution of Mars water profiles over 10 to 55 km altitudes indicate significant departures from current Global Climate Model (GCM) simulations of Mars atmospheric water (Navarro et al., 2014) as also found by Maltagliati et al. (2013). They suggest more complex interactions associated with transport and cloud formation on the spatial and seasonal distributions of Mars atmospheric water than currently modeled (Clancy et al., 2017). Neither of these exploratory Mars water profiling data sets includes coincident temperature retrievals and both are subject to limited spatial/seasonal coverage, particularly in the lower scale height (< 10 km). The lack of simultaneous temperature retrievals is an obstacle to detailed understanding of water ice cloud microphysics, including supersaturation. The lack of water profile sounding in the lower scale height is a particular weakness with respect to comparisons with global water column data sets (e.g., Smith, 2004), which have been widely employed to assess polar cap and sub-surface water ice exchanges with atmospheric water vapor as well as the deep vertical transport of such water vapor cycling within the Mars global atmospheric circulation (Montmessin et al., 2004; Navarro et al., 2014). An ability to make coincident water vapor and temperature profile measurements in the presence of dust and aerosols is particularly important for understanding atmospheric phenomena in the lowermost scale height and within key cloud formation regions such as the polar hoods and the aphelion cloud belt.

A critical aspect in the assessment of condensation enrichment processes (CO), current model-data disagreements in ozone column measurements, and D/H enrichment associated with water vapor condensation that is currently lacking is that of vertically-resolved observations of CO, D/H ratio, and O_3 during the polar night. Both Mars Express and Mars Reconnaissance Orbiter have provided CO measurements, but these

have been column abundances (Encrenaz et al., 2006; Smith et al., 2009). MAVEN does not measure any species below about 100 km, with the exception of column O_3 measurements (Lefévre et al., 2017). The ExoMars Trace Gas Orbiter is likely to be limited in spatial/seasonal vertical profiling (especially at low to mid latitudes) due to its reliance on solar occultations, as is the case with Mars Express. None of the existing (or imminent) atmospheric Mars measurements allow profiling over 5–20 km altitudes reliably in the presence of even modest water ice or dust columns, at times of most interest (dust storms or the aphelion cloud belt).

To gain insight into Martian atmospheric wind fields, water vapor distribution and transport, and to investigate the physical processes controlling them, global-scale and meso-scale atmospheric models have been developed. These models have been validated to the extent possible with the available data, namely, temperature profiles, dust and water ice content, and water vapor column during daytime. In fact, GCMs (e.g., Haberle et al., 1993; Forget et al., 1999; Hartogh et al., 2005) now include most aspects of the Martian climate system: atmospheric dynamics, dust, water and CO_2 cycles, and photochemistry. In particular, GCMs have been used to describe the Mars atmosphere general circulation, i.e., the characteristics of the meridional circulation (Hadley cells) and the role played by the planetary waves (e.g., thermal tides, baroclinic waves, stationary waves, Kelvin waves). Although such models are able to match many of the available temperature data, the same factors that limit the accuracy of simple thermal wind calculations also impact the accuracy of model predictions of wind magnitudes. For instance, using such models, it can be shown that two very similar thermal structures can correspond to very different circulation patterns. In some simulations, a very small temperature difference can induce very large wind changes (Gilli et al., 2017). Clearly wind measurements are necessary to constrain the general atmospheric circulation and the related transport.

Global Climate Models are usually too coarse to represent "mesoscale" meteorological phenomena with horizontal scale below about 200 km, so mesoscale models have been developed to investigate these features (e.g., Rafkin et al., 2001). There are a variety of such mesoscale systems on Mars that are known to be present, or which should be present based on observations, theory, and modeling. These include slope flows (Ye et al., 1990; Savijärvi and Siili, 1993; Rafkin, 2001), dust storms (Cantor, 2007; Cantor et al., 2001; Newman et al., 2002), dusty circulations (Rafkin et al., 2002; Hollingsworth and Kahre, 2010; Toigo, 2002), cloud formation and circulation (Michaels et al., 2006; Montmessin et al., 2004; Wang, 2002), gravity waves (Medvedev et al., 2015), and Kelvin waves (Wilson, 2000). All of these phenomena involve processes that have an impact on one or more observable thermodynamic or kinematic variables.

Slope flows scale roughly with the scale of the topography and have a depth that scales with the boundary layer. For example, the upslope (daytime) phase of the circulation along the topographic dichotomy, large

mons, or along the slopes of large-scale impact craters should be directly observable if the line-of-sight is along the topographic gradient (Figure 1). Local and regional dust storms are also expected to have significant thermal and wind perturbations, and observations of the wind and thermal structure will permit testing of dust storm development mechanisms (Rafkin, 2009; Spiga et al., 2013). In the strongest circulations, the vertical motion is predicted to exceed 10 m/s. Direct confirmation of these strong, deep plumes in dust storms (Rafkin, 2009; Spiga et al., 2013) and along topographic peaks (Rafkin et al., 2002; Rafkin, 2012) is important. The influence of all these phenomena on the distribution of water vapor is uncertain, but, in the absence of condensation processes, water vapor acts as a passive tracer, as it does on Earth (e.g., Mote et al., 1996; Hartogh et al., 2010c; Flury et al., 2013), and as do some other Martian atmospheric constituents. Measurements can therefore further help characterize the circulations.

Gravity waves propagating from lower altitudes are thought to strongly affect the circulation in the middle and upper atmosphere of Mars. Small-scale gravity waves are continuously generated in the troposphere by a variety of meteorological phenomena: flow over topography, convection, instability of jets and fronts. Wave amplitudes grow exponentially as they propagate upwards into increasingly less dense air, and, eventually, the waves either break or are obliterated due to increasing molecular diffusion. The momentum and energy carried by these harmonics is then transferred to the larger-scale flow, providing acceleration/heating or deceleration/cooling. While gravity waves cannot yet be resolved by GCMs, various parameterizations have been applied to tentatively represent their effects. Simulations accounting for orographic gravity waves (Forget et al., 1999; Angelats i Coll et al., 2005) and especially non-orographic gravity waves (Medvedev et al., 2011b, 2015) have shown that their effect on the winds above ~70 km can be very strong. The most spectacular effects are a significant weakening and even reversal of the zonal jets and enhancement of the meridional pole-to-pole circulation. The current estimates of the gravity wave forcing are based on a handful of measurements of small-scale structures in the troposphere provided by Mars Global Surveyor (MGS), Mars Odyssey (ODY), and Mars Reconnaissance Orbiter (MRO). Gravity waves are notoriously difficult to measure due to small amplitudes in the source region (a few Kelvin in temperature and up to 1 m/s in wind). This change in temperature is of the same order as that due to radiative effects in the CO_2 IR bands (Medvedev et al., 2015), while the wind field changes are much more extreme – tens of m/s and even a reversal of the direction of zonal winds (Medvedev et al., 2011a). These theoretical predictions need validation and gravity wave effects can be constrained with global measurements of wind and temperature profiles in the middle and upper atmosphere. In addition, to help quantify such gravity wave impacts on the larger-scale atmosphere, submillimeter limb sounding has also been used to directly measure gravity wave spectra on Earth (Wu and Waters, 1996; Wu and Eckermann, 2008). Such an approach is potentially applicable to the

Martian atmosphere also, and could usefully resolve spectra for horizontal wavelengths as short as ~20 km, depending on the observation geometry.

To understand water vapor distribution, atmospheric circulation, and the influential processes, we demonstrate in this paper that a submillimeter sounder could provide the needed high-precision and resolution, simultaneous vertical profiles of temperature, water vapor and winds, as well as other trace gas species. Measurements, such as these, would enable us to better disentangle the effects of thermal and mechanical forcing mechanisms. In Section 2 we describe the submillimeter sounding technique and background. In Section 3, we discuss the various frequency ranges selected and analyzed. Section 4 describes our measurement simulation approach, with simulation results presented in Section 5. Section 6 discusses how the choice of frequency affects critical instrument parameters such as power and mass. Finally, Section 7 summarizes our findings and reviews the strengths and weaknesses of each potential frequency region.

2. Submillimeter sounding and its potential application to Mars

Passive limb sounding of thermally emitted radiation (from the thermal infrared to the microwave) or scattered sunlight (near infrared through ultraviolet) is a well-established technique for measuring atmospheric composition and other parameters for Earth (e.g., Gille and Russell, 1984; Barath et al., 1993; Aellig et al., 1996; Murtagh et al., 2002; Fischer et al., 2008; Waters et al., 2006), Mars (e.g., McCleese et al., 2007) and other planets. Scanning the instrument field of view vertically across the atmospheric limb enables information to be obtained with greater vertical resolution than is typically attainable with nadir sounding. In addition, the long atmospheric limb path length improves signal to noise for tenuous trace gases by several orders of magnitude compared to nadir viewing geometries. However, that same long path makes the horizontal resolution poorer than is attainable from nadir sounders, at least in the line-of-sight direction. That said, if the instrument looks in the orbital plane, then application of tomographic retrieval techniques (e.g., Livesey and Read, 2000) can improve the resolution somewhat.

Spaceborne microwave and submillimeter limb sounding instruments have a strong heritage in Earth atmospheric composition sounding including the Microwave Limb Sounder (MLS) instruments on NASA's Upper Atmosphere Research Satellite and Aura missions (Barath et al., 1993; Waters et al., 2006), the space shuttle-borne Microwave Atmospheric Sounder (MAS) instrument (Croskey et al., 1992), the Submillimeter Radiometer (SMR) instrument on Odin (Frisk et al., 2003) and the Superconducting Submillimeter-Wave Limb-Emission Sounder (SMILES) on the International Space Station (Kikuchi et al., 2010). Aura MLS, while mainly focused on atmospheric composition measurements, has also been shown to provide information on vertical profiles of mesospheric line-of-sight winds (Limpasuvan et al., 2005; Wu et al., 2008). The

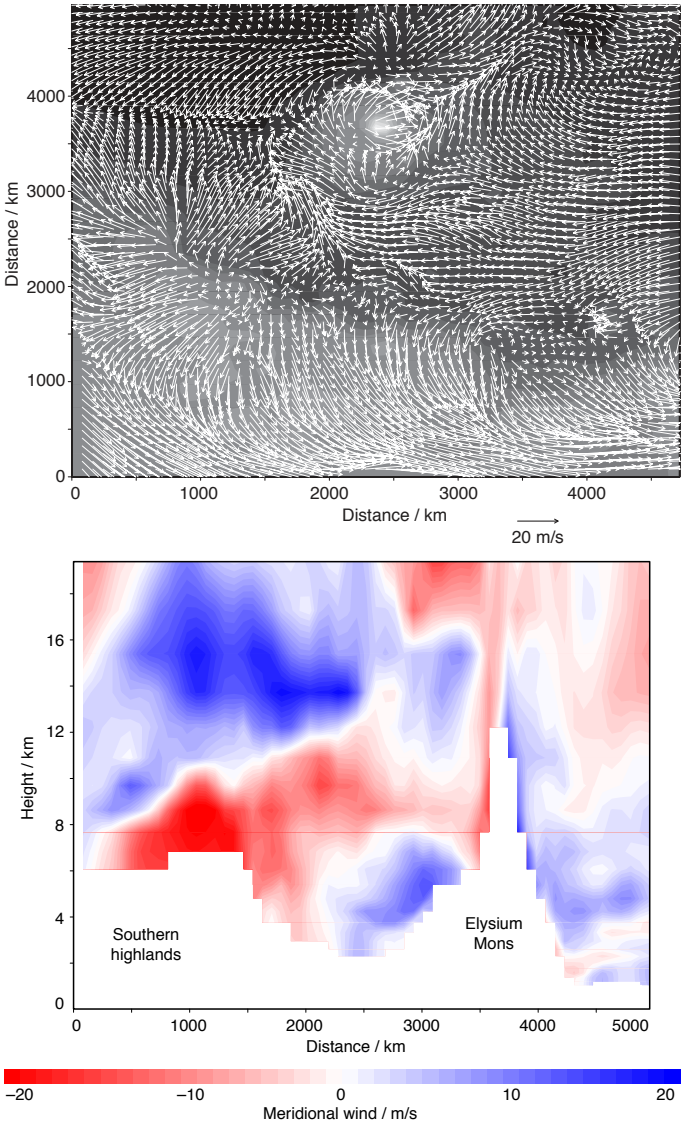

Figure 1: Near-surface winds in the afternoon tend to blow upslope, as shown in mesoscale modeling results along the topographic dichotomy (upper figure). Topography is shaded with high elevations in white. Elysium Mons is the peak in the north central region of the domain. The slope circulations extend well into the lowest scale height of the atmosphere, as shown in the N-S cross-section, below, where red shades are southward blowing winds and blue shades are northward blowing winds. Also evident is the oppositely directed return flow. Near Elysium Mons, there are interactions between the slope flows and mountain waves.

ability of submillimeter limb sounders to make continual near-global observations on a daily basis, including in heavily dust- or aerosol-laden atmospheres, makes such an instrument ideally suited to fill the outstanding observation gaps.

Submillimeter measurements of the Martian atmosphere have been made from ground-based observatories (e.g., Lellouch et al., 1991; Gurwell et al., 2000; Clancy et al., 2004; Hartogh et al., 2007) and from Spaceborne sensors (e.g., Gurwell et al., 2000; Biver et al., 2005; Hartogh et al., 2010a,b; Swinyard et al., 2010). Thus far, however, despite multiple studies (e.g., Forget et al., 2002; Urban et al., 2005; Kasai et al., 2012) and proposed concepts, no such sensor has flown on a Mars-orbiting spacecraft. Recent advances in microwave and submillimeter technology, driven in part by the needs of the communications industry, enable dramatic reductions in mass, power, and volume needed for such instruments, making their deployment to remote planets a realistic and attractive proposition. The subsequent sections review the observations that can be made by a state-of-the-art submillimeter wave limb sounding instrument in Low Mars Orbit, with a specific focus on how the performance of the wind and composition measurements varies with choice of spectral observation region.

3. Radiometer frequency selection

The main measurement objectives are vertical profiles of wind, temperature, and humidity. Wind measurements are best accomplished by measuring strong but sub-opaque lines, ideally having a narrow line width to enable robust quantification of line shifts relative to the line's zero-velocity position. The lines observed do not necessarily need to be from molecules that are well mixed, nor have well-known abundances as, to first order, abundance information (line amplitude) and wind information (line position) are separable. The four isotopes of carbon monoxide have lines meeting these needs well, between them giving useful information from strong but optically thin lines from the surface (where $C^{17}O$ provides the best information) to ~100 km (where CO is the main information source). In addition, the ^{13}CO, and $C^{18}O$ isotopologues provide useful signals over that complete vertical range. Temperature information can be obtained from spectral and altitude regions where the atmosphere is opaque. The CO lines are opaque from the surface up to ~20 km, as are water vapor lines at the surface.

Measurements of HDO, O_3, and H_2O_2 can fulfill additional science objectives. Measurements of the D/H ratio on Mars show that it is significantly enriched compared to Earth (Owen et al., 1988; Krasnopolsky et al., 1997; Webster et al., 2013; Villanueva et al., 2015). Seasonal and diurnal condensation and fractionation cycles involving half of the available atmospheric water vapor abundance may lead to considerable seasonal variations.

Table 1: Target line positions (in GHz) for 6 radiometer frequencies

Molecule	335 GHz	450 GHz	550 GHz	900 GHz	1000 GHz	1130 GHz
$OC^{18}O$	332	441	574	904	1014	1124
CO	346	461	576	922	1037	1152
^{13}CO	331	441	551	881	991	1101
$C^{18}O$	329	439	562	878	988	1097
$C^{17}O$	337	449	562	899	1011	1123
H_2O(s)	325	443	557	916	988	1097
H_2O(w)	321	448	572	906	970	1147
HDO	335	465	560	894	984	1162
$H_2{}^{18}O$	322	NA	548	908	995	1137
O_3	327	441	571	908	1009	1145
H_2O_2	327	446	550	908	1018	1131
Bandwidth / GHz	26	27	29	45	67	68
Bandwidth /% RF	7.7%	6.0%	5.2%	5.0%	6.7%	6.0%

To find candidate regions for these measurements, we have searched the JPL spectral catalogue database `https://spec.jpl.nasa.gov` (Pickett et al., 1998). The requirement was to have the frequencies of the target lines be close enough that, after down conversion by the local oscillator, the Intermediate Frequency (IF) band width could be as small as possible, nominally about ∼5% of the local oscillator frequency. To begin each search, a frequency range dictated by the positions of the $C^{18}O$ (lowest frequency) and CO (highest frequency) lines was considered. This range was then expanded to cover an 8% window centered on the mean frequency of these two lines. Within this range, candidate H_2O, HDO, and $H_2{}^{18}O$ lines were sought. A requirement was that there be at least one strong H_2O line (JPL catalogue strength > -4.0) and one weak H_2O line (JPL catalogue strength between -6.0 and -4.0) present. If a suitably weak H_2O line was not available, a strong $H_2{}^{18}O$ line (JPL catalogue strength > -2.5) was selected for use as a proxy, assuming the telluric isotopic ratio according to VSMOW (Vienna Standard Mean Ocean Water) of about 500, which is a well established ratio for Mars (Webster et al., 2013). The strength ranges were established based on simulation studies, and will allow H_2O to be measured from the surface up to at least 100 km. The other requirement was that an HDO line also exist within the targeted frequency search window. Other targeted molecules, such as ozone, have relatively dense spectra and thus typically have useful lines within

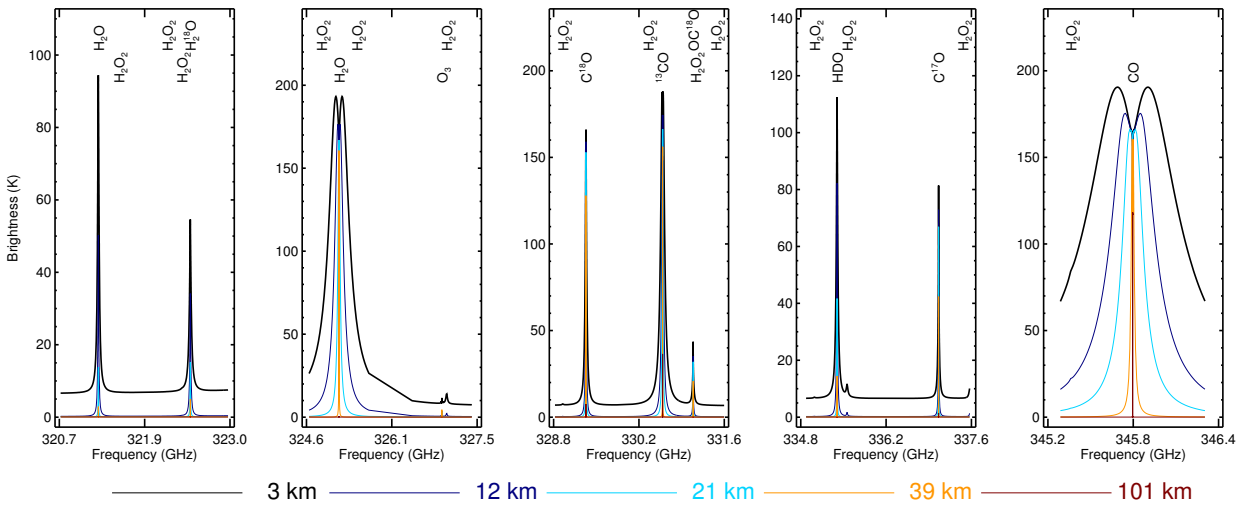

Figure 2: Limb radiative transfer calculations in the 320–350 GHz range for the MCD atmosphere for 17 May 2017, L_s = 154° at 0 UT 0° longitude and 0° latitude. Frequency locations of molecular lines are indicated above the spectrum. Colors show the spectrum for the given limb tangent.

each search window. Frequencies from 0 to 1200 GHz were searched, with the upper frequency limit being based on technological considerations. Table 1 summarizes the results of this search.

Simulated atmospheric signals for these spectral regions have been calculated using a representative Martian atmosphere. The martian atmosphere is taken from the Mars Climate Database (MCD) v5.2, `http://www-mars.lmd.jussieu.fr` for 17 May 2016, L_s = 154° at 0 UT at 0° longitude and 0° latitude. The MCD provides concentrations for all the species except H_2O_2, for which the model L_s = 70° concentration profile (day-night average) published in Encrenaz et al. (2012) is used. Figures 2–7 show key line locations found in the searches described above. As is readily seen, there is a large range of signal strengths available, particularly for H_2O and its isotopologues. Weak lines for molecules such as H_2O_2 and O_3 that are situated closer to strong water vapor lines will be challenging to measure due to the attenuation of the weaker signals by the water vapor absorption.

4. Measurement simulation setup

Although the methods described above readily identify regions of the spectrum where measurement potential exists, more comprehensive calculations are needed to fully assess the strengths and weaknesses of each such spectral region. Specifically we need to quantify the precision and vertical resolution that can be achieved for measurements of wind, temperature, humidity and composition in each case. This is accomplished here by employing the widely-used optimal estimation approach (Rodgers, 2000). For the purposes

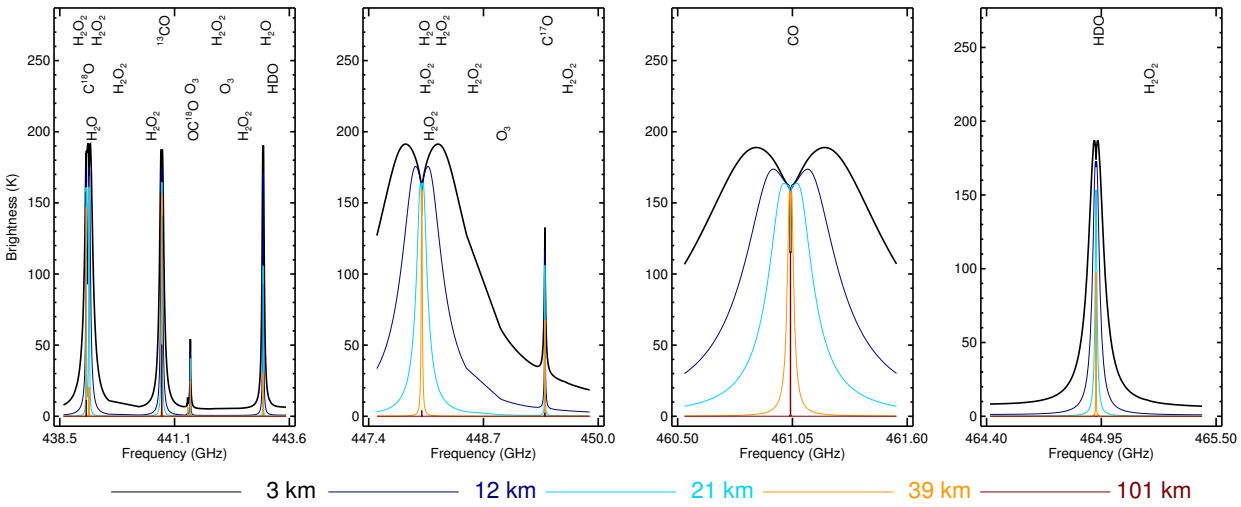

Figure 3: As Figure 2 but for 430–470 GHz.

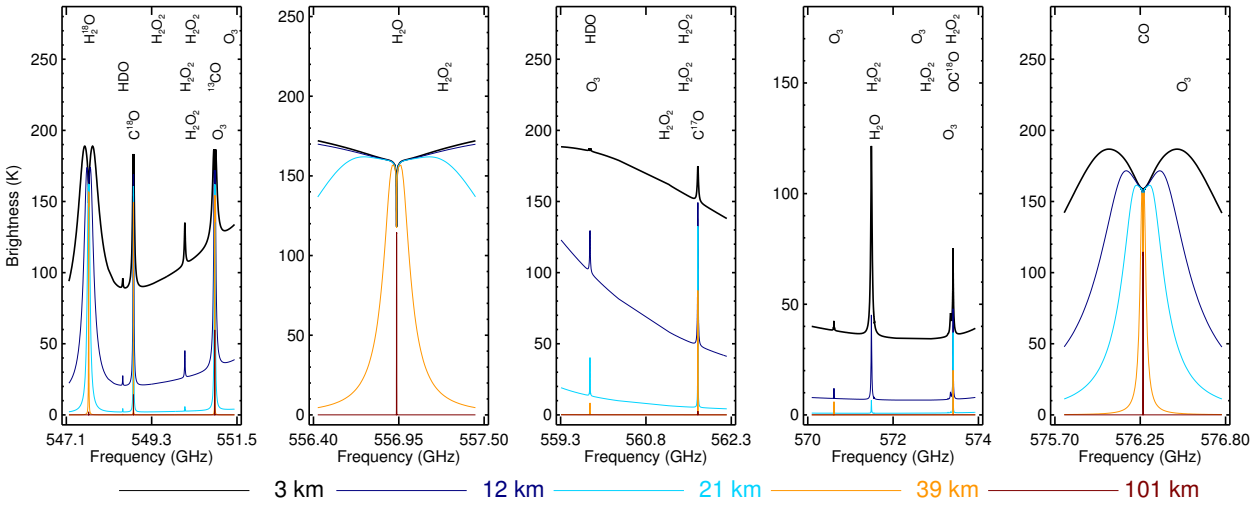

Figure 4: As Figure 2 but for 540–580 GHz.

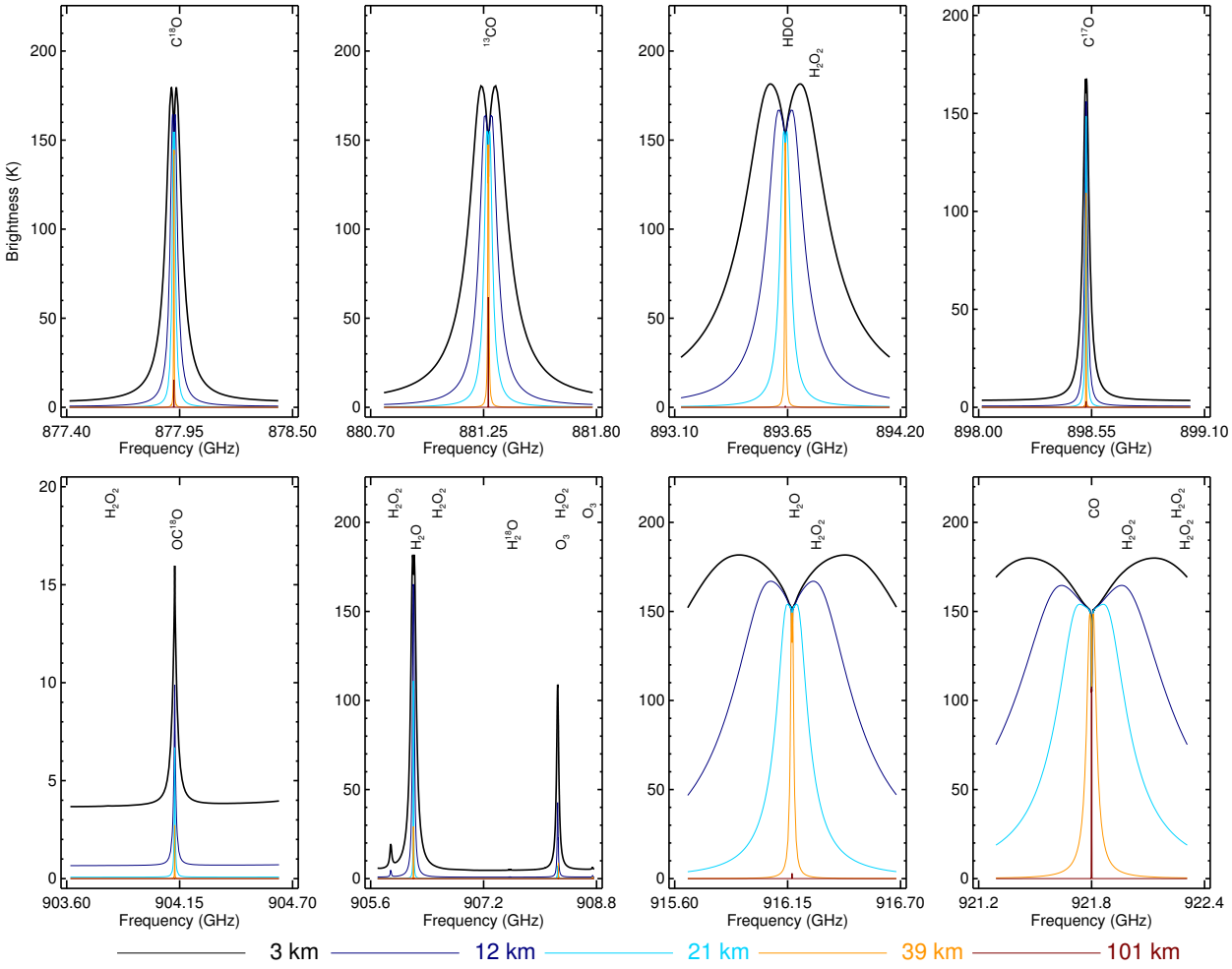

Figure 5: As Figure 2 but for 870–930 GHz.

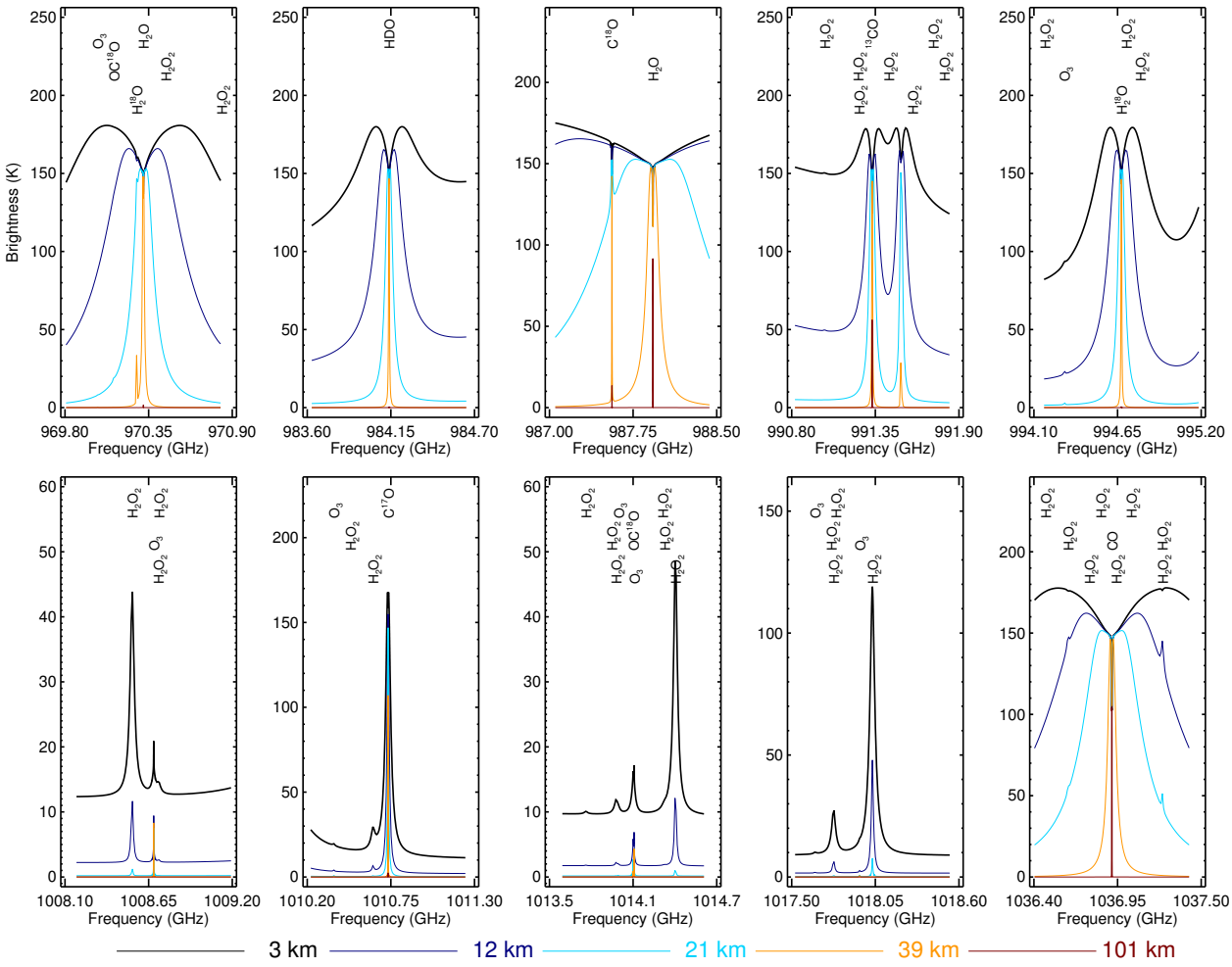

Figure 6: As Figure 2 but for 980–1040 GHz.

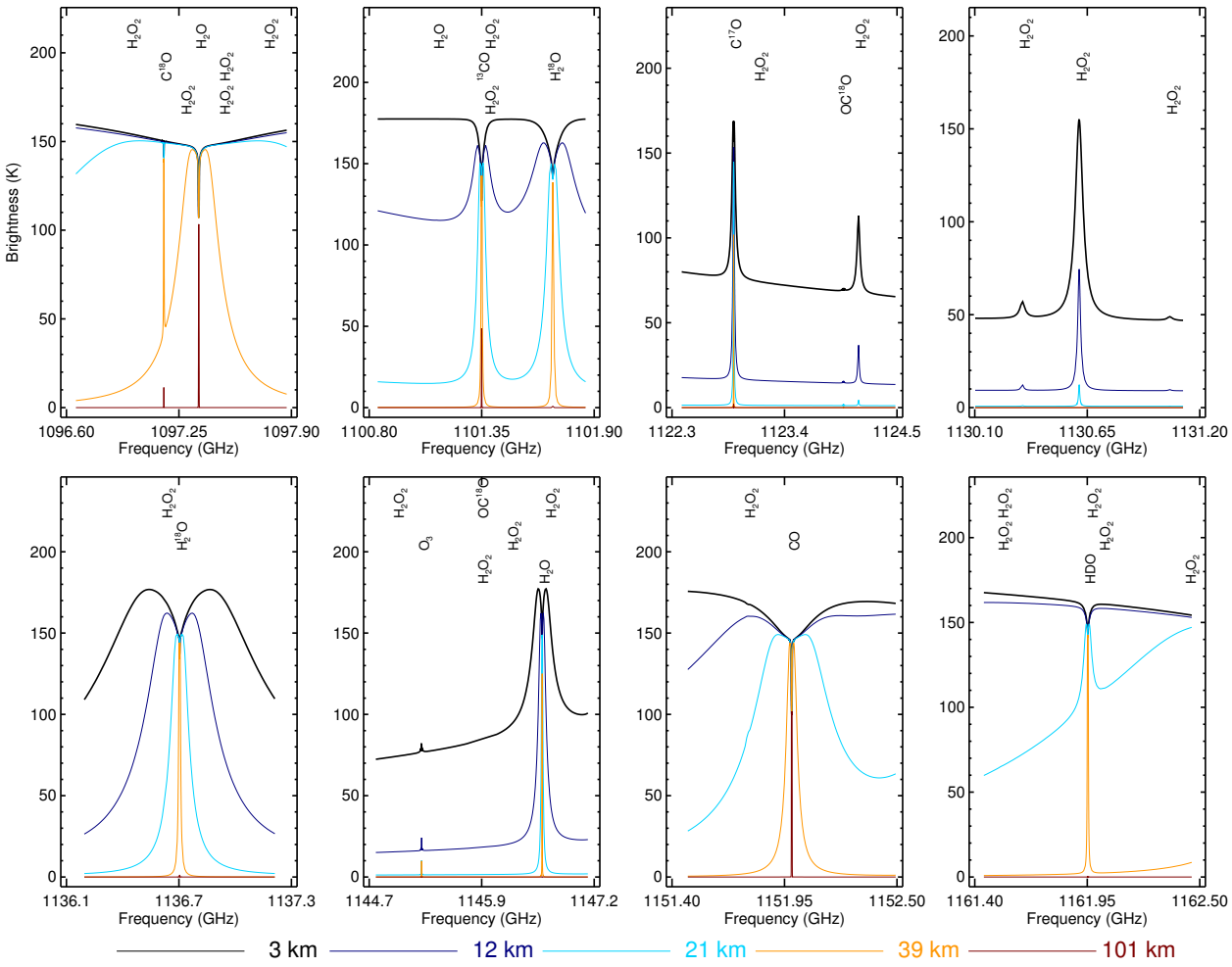

Figure 7: As Figure 2 but for 1090–1170 GHz.

of quantifying potential instrument performance, we do not need to develop a full optimal estimation capability (with non-linear iterative solvers etc.), but the fundamental framework remains the same. Specifically, we construct a "state vector", describing the geophysical data products to be estimated (wind, temperature and composition profiles along with other supporting information), and a "forward model" that estimates the microwave limb radiances that would be observed for a given atmospheric state. The typical task of the retrieval algorithm is then to identify a solution state that best matches (using an error-weighted metric) the observed radiances, along with an estimate of the precision and resolution of that solution. It is only the latter precision/resolution information that is required for our purpose here.

The limb radiance forward model used in this study (Read et al., 2006) is the same as that used for the Aura Microwave Limb Sounder instrument Waters et al. (MLS 2006) project. Specifically, it performs a set of line-by-line radiative transfer calculations over a range of limb-viewing paths. The results of these are then convolved in the vertical with the instrument field of view response, and interpolated to the required limb viewing angles (actually expressed as limb tangent point pressure).

The MLS algorithms have been adapted to use planetary geopotential and ellipse figure models appropriate for Mars. The atmosphere is assumed to be composed of CO_2 (CO_2, ^{18}OCO), CO (CO, ^{13}CO, $C^{18}O$, and $C^{17}O$), H_2O (H_2O, $H_2{}^{18}O$, HDO), O_2, O_3, and H_2O_2. Other trace gases are not considered. The concentrations of these gases are taken from the same MCD profile used in section 3, with H_2O_2 again taken from Encrenaz et al. (2012). Note that Section 5.5 discusses calculations performed for other seasons and regions. Isotopologues are scaled by Earth crustal isotope ratios with adjustments that account for the enrichment in heavier isotopes compared to Earth. Based on sample analysis on the Mars Curiosity Rover, $C^{18}O$ and ^{18}OCO are increased by 5%, $H_2{}^{18}O$ is increased by 8% ^{13}CO by 5%, and HDO by a factor of 5. These values are rounded to the nearest single percentage digit, given the associated measurement uncertainties (Webster et al., 2013). Scattering from dust is negligible at these observing frequencies. Thermal emission from dust has far less spectral variability than molecular line signals, and thus can be treated as a spectrally flat offset. Even in conditions of heavy dust loading, 20 km tangent altitude limb views are subject to only ~6 K brightness temperature enhancement (Kasai et al., 2012), an amount readily accounted for in our simulations, as described below.

The state vector is comprised of single profiles for each of the species listed above, along with a profile of temperature and a profile of wind in the line-of-sight direction. The profiles are described on a 65-level grid using pressure as the vertical coordinate. The first 45 levels are spaced every 2–3 km (equally spaced 0.125 in $\log_{10}[p/\mathrm{hPa}]$), with the following 16 levels spaced at 4–5 km (0.25 in $\log_{10}[p/\mathrm{hPa}]$), and the final two being ~10 km apart (0.5 in $\log_{10}[p/\mathrm{hPa}]$).

The instrument design assumes multiple individual spectrometers centered, where applicable, on each of the targeted molecules above. Each spectrometer has a total bandwidth of 1 GHz, with 256 100 kHz-wide channels in the central portion, flanked by two sets of 64 8 MHz-wide channels, one on each side. The narrow channels provide high spectral resolution for the Doppler shift measurement needed for wind profiling. The broader channels provide lineshape information for obtaining concentration and temperature measurements down to the surface, where possible. In an ultimate instrument design, the precise layout of channels may well differ (with the wider channels assumed here likely to be formed by "ganging together" narrower channels as part of on-board data compression algorithms. However, the configuration modeled here is likely to be representative of the channel distribution that would be chosen.

The instrument field of view is scanned from the surface to 150 km in 76, 2-km steps, with a 1 s integration time for each limb view, giving a total of 76 s for a vertical scan. Horizontal motion of the satellite during the scan is ignored for simplicity here. While it is typically explicitly considered in operational retrieval algorithms (particularly those employing tomographic methods, e.g., Livesey et al., 2006), the impact on the precision and resolution metrics quantified here is negligible. The instrument is assumed to include a 23 cm primary reflector, having an edge taper of 20 dB. For simplicity, the radiative transfer calculations are performed monochromatically for each channel.

The spectroscopy parameters (positions, strengths, ground state energies, and partition functions) are from the JPL catalog (Pickett et al., 1998). Pressure broadening line widths are from the HITRAN catalog (Rothman et al., 2003) or from published literature (Read et al., 2006). The widths in these catalogs are for terrestrial air broadening, and so have been adjusted for broadening by CO_2 (the dominant Martian atmospheric constituent), by multiplying the widths by 1.65, as in Urban et al. (2005), following laboratory measurements of CO broadening by CO_2 (Priem et al., 2000; Varanasi and Tejwani, 1971).

The expected noise levels associated with each simulated radiance measurement are also computed, assuming receiver noise temperatures ($T_{\rm rec}$) of 1400, 1700, 2000, 3600, 4200, and 5000 K for the 335, 450, 550, 900, 1000, 1130 GHz receivers, respectively (single sideband). These estimates are based on performances of state-of-the-art receiver systems (Mehdi et al., 2017) operating in or near these frequency ranges. The noise for each radiance is computed from the radiometer equation as $(T_{\rm scene} + T_{\rm rec})/\sqrt{\Delta\nu\tau}$, where $T_{\rm scene}$ is the incoming signal brightness (~0–250 K depending on channel frequency and instrument pointing), $\Delta\nu$ is the channel width (either 8 MHz or 100 KHz), and τ is the integration time (1 s per limb view).

The retrieval calculation seeks the optimal solution for wind, temperature, and composition, considering information from all spectrometers and all limb viewing angles simultaneously. In support of this calculation

additional quantities are included in the state vector. The most important of these are the limb tangent pressures for each of the 76 limb views in the scan, estimates of which derive from observed pressure-broadened line widths (and from pointing information as described below). Another set of terms in the state vector are additive spectrally flat radiance baselines that are retrieved separately for each scan position (76 total in the vertical scan), with one independent set for each spectrometer. Such terms are used in operational retrievals (Livesey et al., 2006) to absorb spectrally flat errors in the instrument calibration or the forward model, or to account for dust emission as described above. Such radiance offsets, while largely uncorrelated with the signals for wind, temperature, composition, etc., needed to be included in the state vector to provide a best fit to the observed radiances. Finally, the state vector includes a term defining the surface pressure, which is used to establish the lower integration boundary for calculating the geopotential height profile product (computed in post-processing by hydrostatically integrating the retrieved temperature profile).

As with Aura MLS, additional information on both limb view tangent pressures and atmospheric temperature profiles can be obtained by comparing the individual limb view tangent altitudes (deduced from instrument and spacecraft pointing) with the altitudes computed from the temperature profile, limb tangent pressures, and surface pressure information in the state vector, assuming hydrostatic balance. This calculation is embodied in a separate "scan forward model", and individual limb tangent altitudes are assumed known with 30 m precision (within an individual scan). Note that, because the wind, temperature and composition profiles are reported on a pressure grid, they are unaffected by systematic biases in pointing, which affect only the state vector element giving the geopotential height for the surface pressure (and, through hydrostatic integration, the geopotential height profile obtained from that information in conjunction with the temperature profile). Accordingly, the spacecraft location and pointing only need to be known in real time with sufficient absolute accuracy (e.g., five kilometers or better) that the correct altitude range of the limb is scanned so as to avoid wasting valuable integration time on significant overscanning. The 30 m requirement for pointing knowledge precision within an individual scan, described above, corresponds to knowledge of pointing changes within a 76 s vertical scan of 22 arcsec (for a 400 km altitude Mars orbit).

The optimal estimation approach involves combining the information from the instrument with a priori knowledge in an error weighted fashion (Rodgers, 2000). Retrieval of full profiles from the observations alone is typically an ill-posed problem, in part because the measurement system has poor sensitivity to targeted geophysical parameters at the altitude extrema, but also, in some cases, because the measurements provide insufficient information to separate overlapping signatures of different state vector elements (e.g., species with broad spectral lines in close proximity). The a priori information provided to the optimal estimation helps stabilize the retrieval system by adding additional constraints in such cases where the

measurement system performs poorly.

As is typical for limb sounders, the uncertainties on these a priori inputs are set rather large here. We have assumed 100 m/s for wind, and 20 K for temperature at all altitudes, and similarly large (i.e., "loose") values for other species (all included in the plots showing the expected measurement precision discussed below). A second order Tikonov vertical smoothing constraint is added to further stabilize the retrieval, as for Aura MLS (Livesey et al., 2006). This smoothing provides an altitude-resolved constraint on the vertical second derivative of the differences from the retrieved and a priori profiles, thus favoring profiles whose shapes resemble those of the a priori profiles. Here, the weights for these terms (which are expressed in terms of second derivative per integer retrieval level squared, and thus have the same units as the corresponding state vector elements) are set the same as the corresponding a priori uncertainties, which are already chosen to be weakly constraining. Even in a situation where the measurement is providing negligible information (e.g., $OC^{18}O$ above 80 km, see figure 10), the smoothing constraint only reduces the uncertainty by about 10%.

Estimated precisions on the retrieved profiles are taken from the diagonal elements of the solution covariance matrix from the optimal estimation equation. Vertical resolutions are estimated as the full-width at half-maximum of the corresponding averaging kernels (Rodgers, 2000; Livesey et al., 2006). It is important to note that improved precision can be traded for poorer vertical resolution (and vice versa) through adjustment of the Tikhonov smoothing constraint, so it is essential to report both here.

For validation purposes, we have also used the simulation setup described above to repeat the analysis of Urban et al. (2005), using the characteristics they assumed for their 325 GHz instrument (e.g., antenna size, vertical scan, observing frequencies, receiver noise, spectrometer design, a priori uncertainties, etc.). The vertical resolutions obtained for observations of CO, ^{13}CO, H_2O, and HDO agree within ~1 km, typically better, over all the vertical range, with precisions agreeing within ~40% over much of the vertical range. Given the large variability in estimated precision with altitude (often multiple orders of magnitude, as will be seen in the next section), we take the view that this degree of agreement is sufficient to give confidence in the validity of our simulation approach. Remaining differences likely reflect fundamental disparities between the two approaches, particularly in the use of pressure rather than altitude as the vertical coordinate, and in the treatment of vertical smoothing. Temperature performance, while generally agreeing well, was harder to compare meaningfully due to the inclusion of nadir sounding information by Urban et al. (2005).

5. Results

5.1. Wind and temperature

The upper panels of Figure 8 shows the estimated wind uncertainties and vertical resolutions to be expected from the six radiometer choices considered here. The 450, 900, and 1000 GHz frequency choices generally produce the best results, in terms of both precision and resolution, from 3 km to 120 km. A general trend towards improved performance with increasing frequency would be expected given that (1) the Doppler shift scales with observation frequency while pressure broadening effects do not and (2) we have assumed the same antenna size for all configurations, giving a field of view width that narrows with increasing frequency. Overall the best performance is accomplished by the 1000 GHz observations, with precision around 10 m/s from 25–80 km and vertical resolution of 5–6 km over much the same range. For comparison, the Wind Imaging Interferometer (WINDII) on the Upper Atmosphere Research Satellite (UARS) measured the Doppler shift and width of the emission of O(^{1}S) lines in order to profile wind from 80–300 km in Earth's atmosphere, with its best precision being 10 m/s at 95 km (worse at higher and lower altitudes, Gault et al., 1996). The High Resolution Doppler Imager (HRDI) also on UARS measured winds from 10–115 km in the Earth's atmosphere from the atmospheric emssions from the O_2 B and γ bands. Its measurement accuracy was found to be 8–12 m/s (Ortland et al., 1996; Burrage et al., 1996).

The lower panels show the results for temperature profile measurements. Precision of 1–2 K is expected for temperature from the surface to ~40 km for all the configurations. The precisions degrade to 3–6 K at ~90 km with the 550 and 900 GHz configurations providing the best and worst precision, respectively. The vertical resolutions vary with altitude. The best resolution is accomplished by the 1000 and 1300 GHz designs, growing from 2–3 K at the bottom of the atmosphere to ~8–12 K above 80 km with the other frequency choices providing resolution ~1–3 km poorer, depending on altitude and frequency. The estimated precision in surface pressure varies with observation frequency, with the best precision being from 0.005 hPa for 335 GHz and the poorest being 0.012 hPa at 1000 GHz. These uncertainties are equivalent to 10–24 m uncertainty in altitude.

5.2. Water vapor and its isotopologues

The estimated precision and resolution for water vapor and its isotopologues are shown in Figure 9. The horizontal axes for the precision plots are on a logarithmic scale, and the assumed atmospheric abundance profiles are also plotted, in black (with stars overlaid), so as to show how the precision compares to the typical amount of each molecule in the Martian atmosphere. For H_2O, the two highest radiometer frequencies produce the best precision at nearly all heights up to 120 km, although 450 GHz offers the best precision in

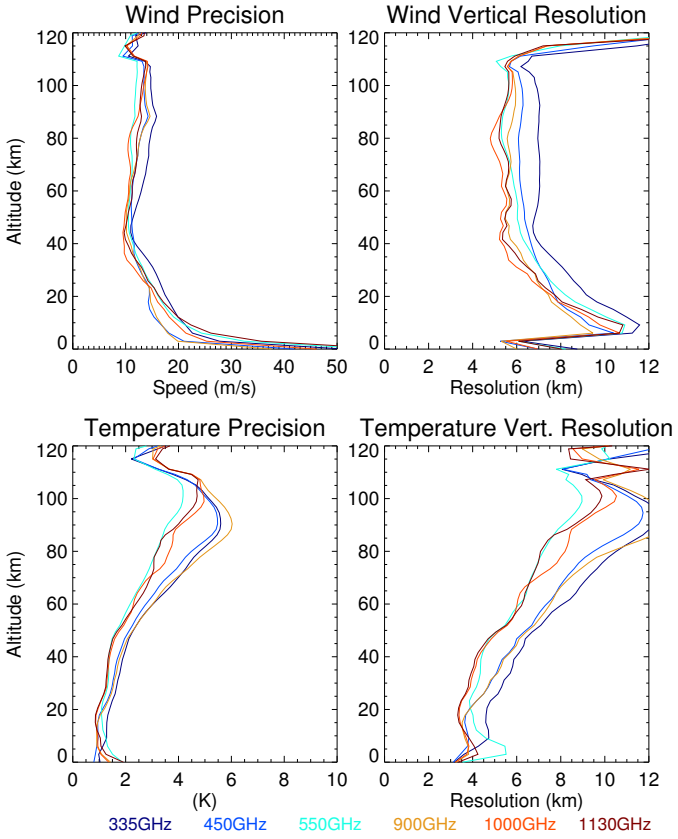

Figure 8: Estimated wind (upper) and temperature (lower) precision (left) and vertical resolution (right) for several frequency ranges considered here. Colored lines correspond to the various radiometer frequencies show below. The expected vertical resolution is based on the full width, half height of the averaging kernel. The a priori uncertainty for wind is 100 m/s with a 10 m/s smoothing constraint. The corresponding numbers for temperature are 20 K and 2 K.

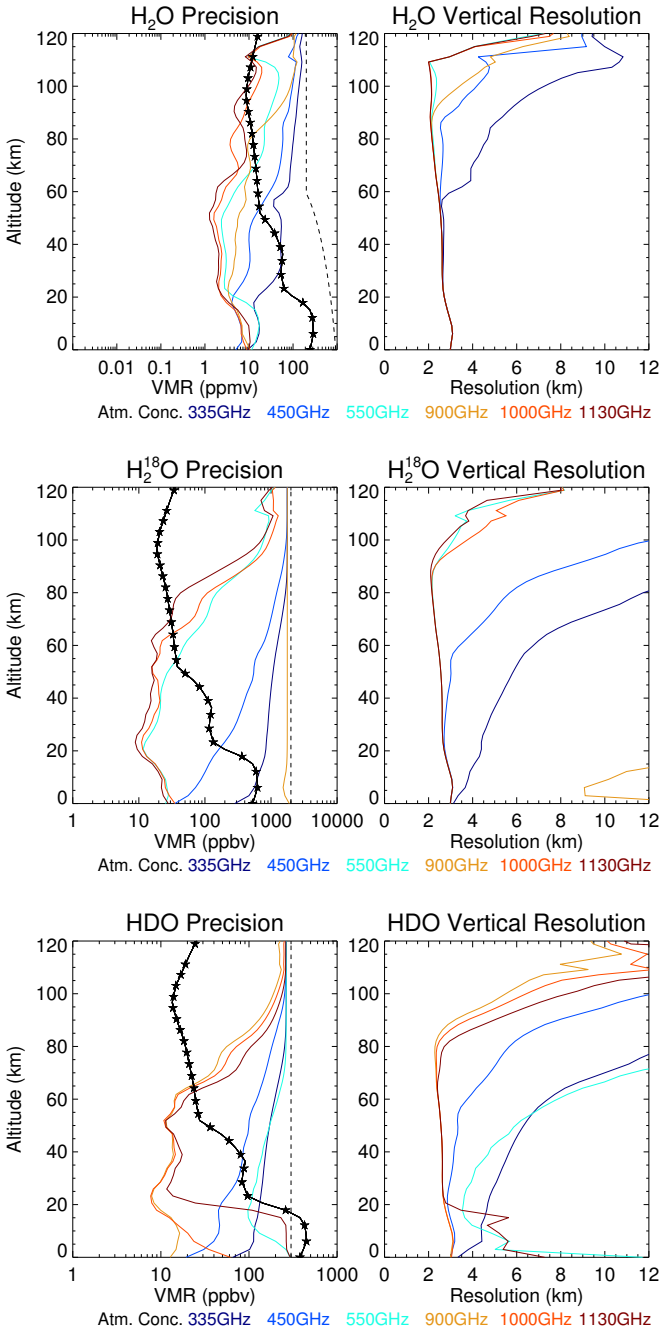

Figure 9: Same as figure 8 for H_2O (upper), $H_2{}^{18}O$ (middle) and HDO (lower). An additional solid black line with asterisks shows the atmospheric concentration assumed each molecule, for comparison. The dashed black lines are the assumed a priori uncertainty. The smoothing constraint is the same as the apriori uncertainty.

the lowest 5 km. The vertical resolution is limited only by the grid point spacing of the profile in this simulation. It gets slightly better with increasing altitude because the gridding is evenly spaced in log pressure and scales with the scale height, which decreases as the atmospheric temperature cools.

The main purpose of including $H_2{}^{18}O$ molecule (middle panels) is to provide a weak humidity line choice where one doesn't exist for a given radiometer. This provides a near surface humidity measurement for the 550 GHz radiometer choice. It is generally believed that the isotopic ratio between ^{18}O and ^{16}O is 1/500 and known to 5% (Webster et al., 2013). It is worth noting that the 550, 1000, and 1130 GHz configurations have better than 5% precision near the surface so additional information about isotopic fractionation can be learned from this measurement (excepting 550 GHz because it does not have a useful near surface H_2O measurement).

The strengths of available HDO lines within the radiometer choices are quite varied, and this is reflected by the associated uncertainties shown in the lower panels of Figure 9. The best choice is the 900 GHz radiometer. The available line in the 1000 GHz radiometer is starting to become opaque near the surface and the 1130 GHz line is stronger still and becomes opaque just below 15 km.

5.3. Carbon species

Figure 10 shows the estimated uncertainties for the various carbon species considered. CO measurements are best made with any of the highest three frequency radiometer regions except near the surface where the lower frequency options are better. The higher frequency CO lines become opaque near the surface. The vertical resolution of the CO measurement is close to the profile representation grid spacing from 0–110 km for the 900 and 1000 GHz frequency choices. The 1152 GHz CO line becomes opaque starting below 20 km and therefore its vertical resolution degrades rapidly. The three lower frequency choices have poorer vertical resolution above 60 km.

The measurement of ^{13}CO has similar characteristics to those of the most abundant CO isotope. The 900 GHz radiometer choice appears best for this molecule in terms of precision and vertical resolution. The best radiometer choice for measuring $C^{18}O$ is 900 GHz. $C^{18}O$ is heavily interfered by strong H_2O lines at 1000 and 1130 GHz and therefore can not be measured well in the lower atmosphere until the nearby H_2O line becomes optically thin.

The $C^{17}O$ molecule is best measured by the highest three radiometer frequencies. Above 60 km however, the atmospheric concentration is less than the estimated precision. The vertical range where useful $C^{17}O$ measurements can be made is rather limited for the three lower frequencies.

For $OC^{18}O$, the 450 GHz line is the strongest and therefore has the best precision. The lines become

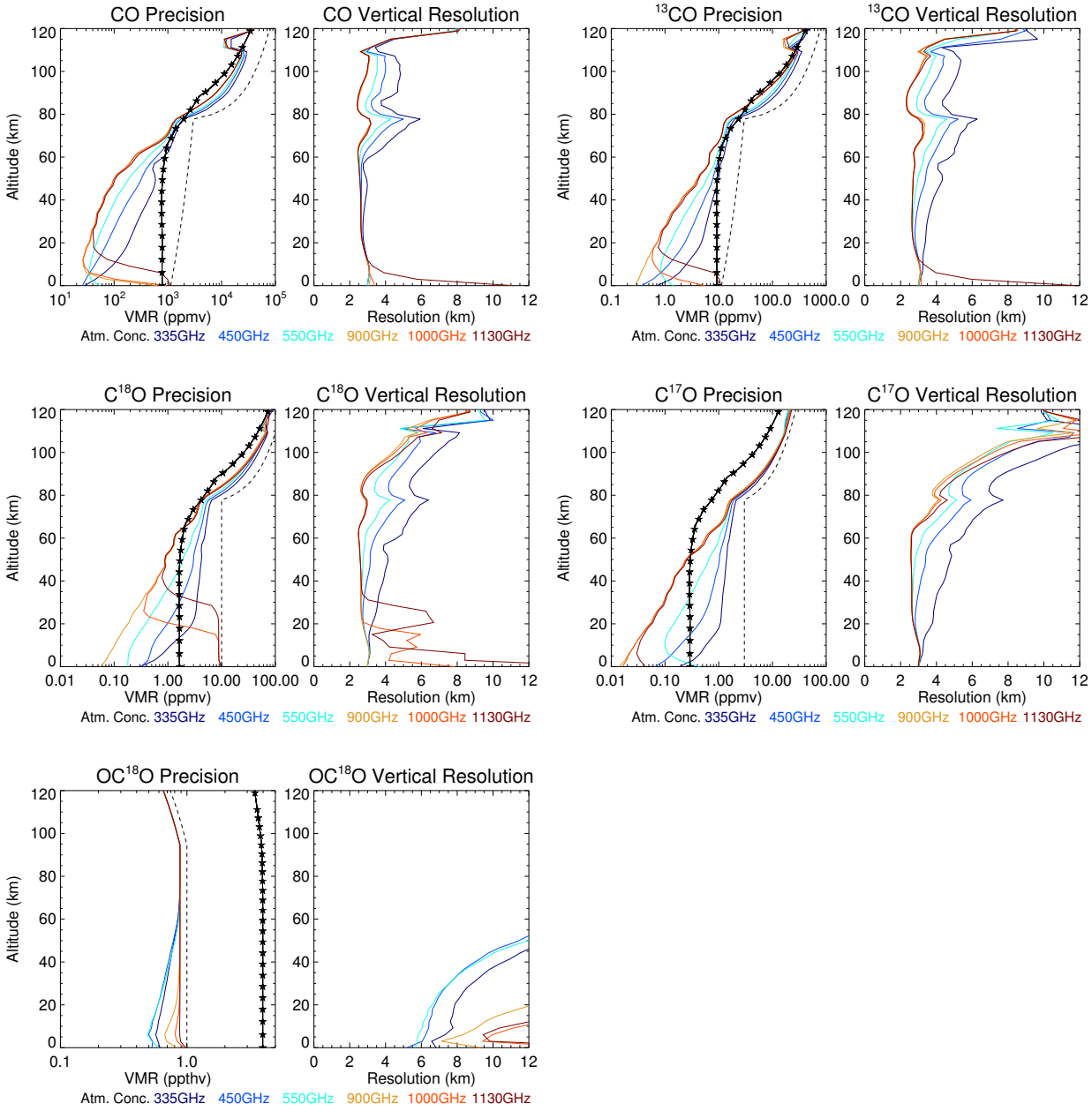

Figure 10: Same as figure 9 for CO, ^{13}CO, C^{18}O, C^{17}O, and OC^{18}O.

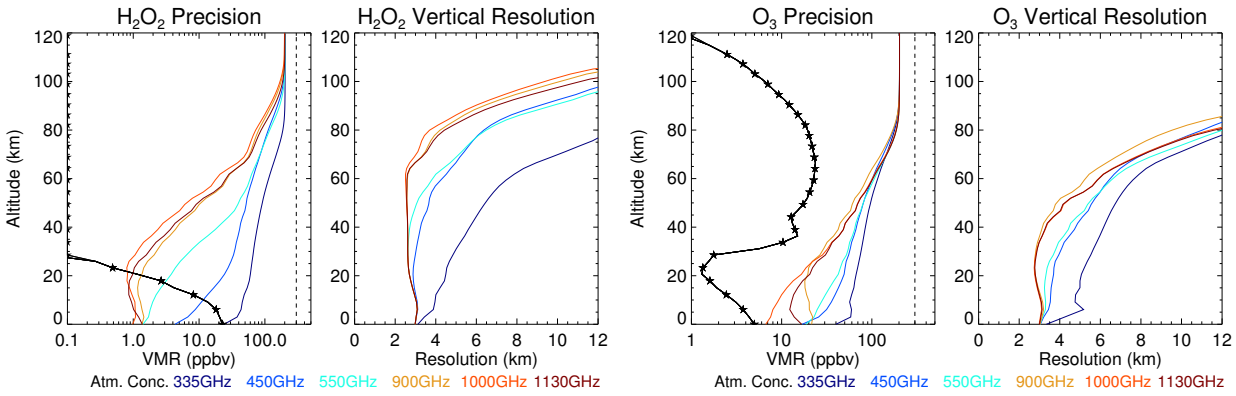

Figure 11: Same as figure 9 for H_2O_2 (left two panels) and O_3 (right two panels).

weaker as frequency is increased or lowered relative to 450 GHz. The nominal concentration is 4 parts per thousand volume (ppthv) so this molecule can be measured with a precision of ~12–15% near the surface in the lower three frequency configurations.

5.4. H_2O_2 and O_3

The left hand two panels of Figure 11 show the estimated H_2O_2 uncertainties and vertical resolutions to be expected from the six radiometer choices considered here. The strongest lines for this molecule are in the 1 THz region, hence the three upper radiometer frequency choices are the best. As seen in the right hand two panels of Figure 11, the single measurement precision for ozone is poor compared to the amount expected in the atmosphere.

5.5. Sensitivity to Martian Humidity

Figure 12 shows how the precisions and resolutions are affected by location and season for the representative case of the 1000 GHz configuration (other configurations exhibit similar behavior). These changes mainly derive from the humidity differences between each case. As one extreme case, the northern hemisphere winter (L_s = 270°, green) is shown, with very dry conditions near the surface. Northern Summer (L_s = 90°, red) represents a more moist case. Also shown is the nominal study case used above (L_s = 154°) which is late northern summer and has humidity between the northern summer and fall cases. Under the driest conditions, humidity can be measured with ~10% precision.

Temperature measurements exhibit very little seasonal or regional variations within the cases shown here. The ability to measure wind is more impacted, notably for the northern hemisphere summer case, for which measurement precision is poor below ~10 km (as is the vertical resolution). The other two cases provide better than 25 m/s precision down to ~5 km. The vertical resolution of water vapor measurements

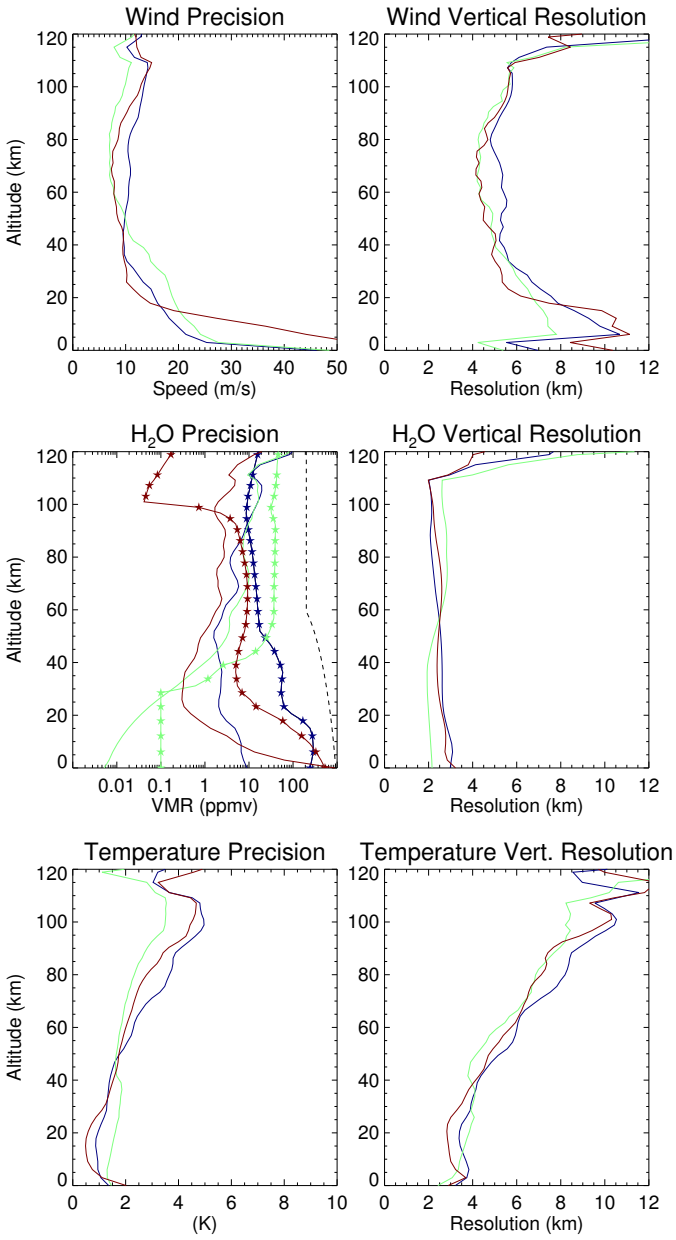

Figure 12: The left panels show error estimates for wind (upper), H_2O (middle) and Temperature (lower) with varying concentration of H_2O in the Martian atmosphere, all using the 1000 GHz measurement. Blue is the equatorial case used in the studies above (L_s = 154°), red is northern hemisphere Summer (L_s = 90°) at 90°N which was chosen to represent maximum water column abundance conditions, and green is northern hemisphere Winter (L_s = 270°) at the north pole, which was chosen to represent minimum water column abundance conditions. The corresponding atmospheric abundance profiles for water vapor are shown as lines with colored stars overlaid to indicate which profile goes with which error estimate. The a priori uncertainties (black dashed lines) and smoothing are unchanged for each profile used. The right panels show the corresponding vertical resolutions.

Table 2: Instrument subsystem power needs for the various radiometer frequencies

Frequency	335, 450, 550 GHz	900 GHz	1000, 1130 GHz
(Intermediate frequency bandwidth	26, 27, 29 GHz	45 GHz	67, 68 GHz)
Local Oscillator Chain	8 W	10 W	13 W
Intermediate Frequency Processor	16 W	24 W	36 W
2nd Downconversion	5 W	7 W	9 W
Spectrometers	16 W	16 W	16 W
C&DH etc.	5 W	5 W	5 W
Total:	50 W	62 W	79 W

is somewhat improved in the northern winter case, being ~2 km from the surface to ~50 km compared with up to ~3 km for the two other cases. This improvement in resolution, which (as described above) is set by the spacing of the retrieval levels, simply reflects the impact of the lower temperature on the vertical spacing of those levels (being constant in log-pressure). The precision of water vapor measurements roughly scales with the water vapor abundance, typically offering a signal to noise ratio of ten to one or better. The only significantly noisier cases are seen around 25 km altitude in northern winter, and in the lowermost ~5 km during northern summer.

6. Implications for instrument requirements

The discussion thus far has focused on the scientific implications of different frequency range choices. Naturally, the choice of frequency has implications for the instrument design and therefore, crucially for planetary missions, mass and power. Based on experience with prior instruments, we are confident that such an instrument, at any of the frequencies identified here, could be accommodated within a 25 kg mass budget (depending on the choice of antenna and scan mechanism; unmargined). The amount of instrument power needed, however, varies strongly with frequency chosen.

For the 335, 450 and 550 GHz choices, where the spectral regions to be covered are ~30 GHz across, we estimate a total of 50 W would be needed (not including margin, which is typically assumed to be 40% for planetary missions). Table 2 details the subsystem-level contributions to this total. For a 900 GHz instrument, the total increases to 62 W. This due mainly to increased power needed to handle the broader Intermediate Frequency range, with contributions from the associated changes to the 2nd Local Oscillator, and from an increase in the power needed for the first Local Oscillator. At the two highest frequencies

considered, 1000 and 1130 GHz, the total increases to 79 W, again driven mainly by the need for a more complex Intermediate Frequency processor, given the larger bandwidth. Given that all the configurations are targeting roughly the same number of spectral lines, the data rate needs are unaffected by choice of frequency. Assuming an instrument comprised of ten 384-channel spectrometers (see discussion above) and a 1 s integration time, the total rate can likely be kept within 100 kbps. Should it be needed, judiciously chosen compression schemes (involving geophysically aware ganging of adjacent channels in a tangent-height-dependent manner) could likely achieve a reduction in that datarate by a factor of 5 or more.

7. Summary of Findings

The six spectral regions considered in Section 5 each offer advantages and disadvantages that must be weighed when considering potential instrument designs. If the scientific focus is on measurements of wind above ~20 km, then the three highest frequencies considered (900, 1000, and 1130 GHz) offer the best performance, particularly in terms of vertical resolution (typically 6 km vs. 7–9 km for the lower frequency measurements), with precision being around 10–15 m/s. Lower in the atmosphere, precision worsens to between 20–40 m/s down to 5 km altitude, poorer still below, with the 450 GHz measurements offering comparable precision to the three high-frequency cases. The generally improved performance with increasing frequency derives from the increase in the magnitude of the Doppler shift (which is proportional to frequency) compared to the pressure broadened width (below 30–40 km), along with increased line strengths (e.g., for H_2O, CO, and their isotopologues). Another contributor to the improved high frequency performance derives from our assumption (given the typical constraints in instrument design) that the same size antenna can be used for all observing frequencies, giving a field of view width that narrows with increasing frequency. This same factor likely also contributes to the generally finer vertical resolution obtained by with higher frequency configurations for temperature and composition measurements. As with wind, temperature and water vapor measurements are best made at higher frequencies, as are measurements in the ~20–80 km altitude range for most trace gas species. The only notable exception to this general performance improvement with higher observing frequency appears to be for some of the composition measurements at the lowermost altitudes. For example, measurements of CO below ~5 km have very poor signal to noise at 900, 1000 and 1130 GHz, with individual profiles having precision comparable to the expected values. Measurements at 450 and 550 GHz by contrast have a single-profile precision of around 2.5%.

Naturally, technology and engineering considerations come in to play when considering instrument design also. While receiver technologies in the THz region are relatively mature, obtaining the needed Local Oscillator (LO) signals within the tight electrical power budgets typical of planetary missions may present

a challenge. The wider IF bandwidth associated with some of the choices (e.g., 68 GHz for 1130 GHZ) will complicate the design of downstream spectral analysis, placing more challenging requirements on secondary down-converters and associated oscillators.

This study follows on from those of Muhleman and Clancy (1995); Hartogh (1998); Forget et al. (2002); Urban et al. (2005); Kasai et al. (2012) who have quantified the performance of comparable instruments. Those studies demonstrate a sustained interest in the application of submillimeter limb sounding to the Martian atmosphere. Given the continuing emphasis on the needs for wind and vertical water vapor observations by the the Mars atmosphere research community, it can be hoped that such an instrument will ultimately materialize. This study assesses the potential capabilities of different instrument configurations and indicates that, technology considerations permitting, higher observing frequencies generally provide more precise and finer resolution measurements.

Acknowledgements

Research carried out at the Jet Propulsion Laboratory, California Institute of Technology, was performed under a contract with the National Aeronautics and Space Administration.

References

C. P. Aellig, N. Kämpfer, C. Rudin, R. M. Bevilacqua, W. Degenhardt, P. Hartogh, C. Jarchow, K. Künzi, J. J. Olivero, C. Croskey, and et al. Latitudinal distribution of upper stratospheric ClO as derived from space borne microwave spectroscopy. *Geophys. Res. Lett.*, 23(17):2321–2324, 1996. doi:10.1029/96gl01215.

M. Angelats i Coll, F. Forget, M. A. López-Valverde, and F. González-Galindo. The first mars thermospheric general circulation model: The martian atmosphere from the ground to 240 km. *Geophys. Res. Lett.*, 32 (4):L04201, 2005. doi:10.1029/2004gl021368.

D. T. Baird, R. H. Tolson, S. Bougher, and B. Steers. Zonal wind calculations from mars global surveyor accelerometer and rate data. *Journal of Spacecraft and Rockets*, 44(6):1180–1187, 2007. doi:10.2514/1.28588.

F. T. Barath, M. C. Chavez, R. E. Cofield, D. A. Flower, M. A. Frerking, M. B. Gram, W. M. Harris, J. R. Holden, R. F. Jarnot, W. G. Kloezeman, G. J. Klose, G. K. Lau, M. S. Loo, B. J. Maddison, R. J. Mattauch, R. P. McKinney, G. E. Peckham, H. M. Pickett, G. Siebes, F. S. Soltis, R. A. Suttie, J. A. Tarsala, J. W. Waters, and W. J. Wilson. The Upper Atmosphere Research Satellite Microwave Limb Sounder Experiment. *J. Geophys. Res.*, 98(D6):10,751–10,762, 1993. doi:10.1029/93JD00798.

N. Biver, A. Lecacheux, T. Encrenaz, E. Lellouch, P. Baron, J. Crovisier, U. Frisk, Å. Hjalmarson, M. Olberg, A. Sandqvist, and S. Kwok. Wide-band observations of the 557 GHz water line in mars with odin. *Astron. and Astrophys.*, 435(2):765–772, 2005. doi:10.1051/0004-6361:20042247.

M. D. Burrage, W. R. Skinner, D. A. Gell, P. B. Hays, A. R. Marshall, D. A. Ortland, A. H. Manson, S. J. Franke, D. C. Fritts, P. Hoffman, C. McLandress, R. Niciejewski, F. J. Schmidlin, G. G. Shepherd, W. Singer, T.Tsuda, and R. A. Vincent. Validation of mesosphere and lower thermosphere winds from the High Resolution Doppler Imager on UARS. *J. Geophys. Res.*, 101(D6):10365–10392, 1996.

B. A. Cantor. MOC observations of the 2001 mars planet-encircling dust storm. *Icarus*, 186(1):60–96, 2007. doi:10.1016/j.icarus.2006.08.019.

B. A. Cantor, P. B. James, M. Caplinger, and M. J. Wolff. Martian dust storms: 1999 mars orbiter camera observations. *J. Geophys. Res.*, 106(E10):23653–23687, 2001. doi:10.1029/2000je001310.

R. Clancy, B. Sandor, and G. Moriarty-Schieven. A measurement of the 362 GHz absorption line of Mars atmospheric H_2O_2. *Icarus*, 168(1):116–121, 2004. doi:10.1016/j.icarus.2003.12.003.

R. T. Clancy, M. J. Wolff, F. Lefèvre, B. A. Cantor, M. C. Malin, and M. D. Smith. Daily global mapping of mars ozone column abundances with MARCI UV band imaging. *Icarus*, 266:112–133, 2016. doi:10.1016/j.icarus.2015.11.016.

R. T. Clancy, M. D. Smith, F. Lefèvre, T. H. McConnochie, B. J. Sandor, M. J. Wolff, S. W. Lee, S. L. Murchie, A. D. Toigo, H. Nair, and T. Navarro. Vertical profiles of Mars 1.27 μm O_2 dayglow from MRO CRISM limb spectra: Seasonal/global behaviors, comparisons to LMDGCM simulations, and a global definition for Mars water vapor profiles. *Icarus*, 293:132–156, 2017. doi:10.1016/j.icarus.2017.04.011.

C. L. Croskey, N. Kämpfer, R. Bevilacqua, G. K. Hartmann, K. F. Künzi, P. R. Schwartz, J. J. Olivero, S. E. Puliafito, C. Aellig, G. Umlauft, W. B. Waltman, and W. Degenhardt. The Millimeter Wave Atmospheric Sounder (MAS): A shuttle-based remote sensing experiment. *IEEE Trans. Microwave Theory and Techniques*, 40(6), 1992.

G. Crowley and R. H. Tolson. Mars thermospheric winds from mars global surveyor and mars odyssey accelerometers. *Journal of Spacecraft and Rockets*, 44(6):1188–1194, 2007. doi:10.2514/1.28625.

T. Encrenaz, T. Fouchet, R. Melchiorri, P. Drossart, B. Gondet, Y. Langevin, J.-P. Bibring, F. Forget, and B. Bézard. Seasonal variations of the martian CO over hellas as observed by OMEGA/Mars Express. *Astronomy & Astrophysics*, 459(1):265–270, 2006. doi:10.1051/0004-6361:20065586.

T. Encrenaz, T. Greathouse, F. Lefèvre, and S. Atreya. Hydrogen peroxide on mars: Observations, interpretation and future plans. *Planetary and Space Science*, 68(1):3–17, 2012. doi:10.1016/j.pss.2011.03.019.

T. Encrenaz, T. K. Greathouse, F. Lefi£¡vre, F. Montmessin, F. Forget, T. Fouchet, C. DeWitt, M. J. Richter, J. H. Lacy, B. Bézard, and et al. Seasonal variations of hydrogen peroxide and water vapor on Mars: Further indications of heterogeneous chemistry. *Astron. & Astrophys.*, 578:A127, 2015. doi:10.1051/0004-6361/201425448.

A. Fedorova, O. Korablev, J.-L. Bertaux, A. Rodin, F. Montmessin, D. Belyaev, and A. Reberac. Solar infrared occultation observations by spicam experiment on mars-express: Simultaneous measurements of the vertical distributions of H_2O, CO_2 and aerosol. *Icarus*, 200(1):96–117, 2009. doi:10.1016/j.icarus.2008.11.006.

H. Fischer, M. Birk, C. Blom, B. Carli, M. Carlotti, T. von Clarmann, L. Delbouille, A. Dudhia, D. Ehhalt, M. Endemann, J. M. Flaud, R. Gessner, A. Kleinert, R. Koopman, J. Langen, M. López-Puertas, P. Mosner, H. Nett, H. Oelhaf, G. Perron, J. Remedios, M. Ridolfi, G. Stiller, and R. Zander. MIPAS: an instrument for atmospheric and climate research. *Atmos. Chem. Phys.*, 8(8):2151–2188, 2008. doi:10.5194/acp-8-2151-2008.

T. Flury, D. L. Wu, and W. G. Read. Variability in the speed of the Brewer-Dobson circulation as observed by Aura/MLS. *Atmos. Chem. Phys.*, 13(9):4563–4575, 2013. doi:10.5194/acp-13-4563-2013.

F. Forget, F. Hourdin, R. Fournier, C. Hourdin, O. Talagrand, M. Collins, S. R. Lewis, P. L. Read, and J.-P. Huot. Improved general circulation models of the martian atmosphere from the surface to above 80 km. *J. Geophys. Res.*, 104(E10):24155–24175, 1999. doi:10.1029/1999je001025.

F. Forget, G. Beaudin, A. D. P. Encrenaz, M. Gheudin, B. Thomas, M. Capderou, K. Dassas, P. Ricaud, J. Urban, M. F. S. Gulkis, M. Janssen, L. Riley, T. Encrenaz, E. Lellouch, and P. H. T. Clancy. Microwave Sounding Of The Martian Atmosphere With Mambo. In *EGS General Assembly Conference Abstracts*, volume 27 of *EGS General Assembly Conference Abstracts*, 2002. URL `http://adsabs.harvard.edu/abs/2002EGSGA..27.4727F`.

U. Frisk, M. Hagström, J. Ala-Laurinaho, S. Andersson, J.-C. Berges, J.-P. Chabaud, M. Dahlgren, A. Emrich, H.-G. Florén, G. Florin, M. Fredrixon, T. Gaier, R. Haas, T. Hirvonen, Å. Hjalmarsson, B. Jakobsson, P. Jukkala, P. S. Kildal, E. Kollberg, J. Lassing, A. Lecacheux, P. Lehikoinen, A. Lehto, J. Mallat, C. Marty, D. Michet, J. Narbonne, M. Nexon, M. Olberg, A. O. H. Olofsson, G. Olofsson, A. Origné,

M. Petersson, P. Piironen, R. Pons, D. Pouliquen, I. Ristorcelli, C. Rosolen, G. Rouaix, A. V. Räisänen, G. Serra, F. Sjöberg, L. Stenmark, S. Torchinsky, J. Tuovinen, C. Ullberg, E. Vinterhav, N. Wadefalk, H. Zirath, P. Zimmermann, and R. Zimmermann. The Odin satellite; I. radiometer design and test. *Astron. & Astrophys.*, 402(3):L27–L34, 2003. doi:10.1051/0004-6361:20030335.

W. A. Gault, G. Thuillier, G. G. Shepherd, S. P. Zhang, R. H. Wiens, W. E. Ward, C. Tai, B. H. Solheim, Y. J. Rochon, C. McLandress, C. Lathuillere, V. Fauliot, M. Hersé, C. H. Hersom, R. Gattinger, L. Bourg, M. D. Burrage, S. J. Franke, G. Hernandez, A. Manson, R. Niciejewski, and R. A. Vincent. Validation of O(^{1}S) wind measurements by WINDII: the WIND Imaging Interferometer on UARS. *J. Geophys. Res.*, 101(D6):10405–10430, 1996.

J. C. Gille and J. M. Russell, III. The Limb Infrared Monitor of the Stratosphere: Experiment description, performance and results. *J. Geophys. Res.*, 89(D4):5125–5140, 1984. doi:10.1029/JD089iD04p05125.

G. Gilli, F. Forget, A. Spiga, T. Navarro, L. Montabone, and E. Millour. On the Impact of Non-Orographic Gravity Waves in the LMD Mars Global Climate Model. In F. Forget and M. Millour, editors, *The Mars Atmosphere: Modelling and observation*, page 2104, 2017. URL `http://adsabs.harvard.edu/abs/2017mamo.conf.2104G`.

R. Greeley, A. Skypeck, and J. B. Pollack. Martian aeolian features and deposits: Comparisons with general circulation model results. *J. Geophys. Res.*, 98(E2):3183–3196, 1993. doi:10.1029/92je02580.

M. A. Gurwell, E. A. Bergin, G. J. Melnick, M. L. N. Ashby, G. Chin, N. R. Erickson, P. F. Goldsmith, M. Harwit, J. E. Howe, S. C. Kleiner, D. G. Koch, D. A. Neufeld, B. M. Patten, R. Plume, R. Schieder, R. L. Snell, J. R. Stauffer, V. Tolls, Z. Wang, G. Winnewisser, and Y. F. Zhang. Submillimeter Wave Astronomy Satellite Observations of the Martian atmosphere: Temperature and vertical distribution of water vapor. *Astrophys. J. Lett.*, 539(2):L143, 2000.

R. M. Haberle, J. B. Pollack, J. R. Barnes, R. W. Zurek, C. B. Leovy, J. R. Murphy, H. Lee, and J. Schaeffer. Mars atmospheric dynamics as simulated by the NASA Ames General Circulation Model: 1. the zonal-mean circulation. *J. Geophys. Res.*, 98(E2):3093–3123, 1993. doi:10.1029/92je02946.

P. Hartogh. Solar system research with microwaves. In *Remote Sensing Methodology for Earth Observation and Planetary Exploration*, pages 23–32. ESA, 1998.

P. Hartogh, A. S. Medvedev, T. Kuroda, R. Saito, G. Villanueva, A. G. Feofilov, A. A. Kutepov, and

U. Berger. Description and climatology of a new general circulation model of the martian atmosphere. *Journal of Geophysical Research*, 110(E11), 2005. doi:10.1029/2005je002498.

P. Hartogh, A. S. Medvedev, and C. Jarchow. Middle atmosphere polar warmings on mars: Simulations and study on the validation with sub-millimeter observations. *Planetary and Space Science*, 55(9):1103–1112, 2007. doi:10.1016/j.pss.2006.11.018.

P. Hartogh, M. I. Błęcka, C. Jarchow, H. Sagawa, E. Lellouch, M. de Val-Borro, M. Rengel, A. S. Medvedev, B. M. Swinyard, R. Moreno, T. Cavalié, D. C. Lis, M. Banaszkiewicz, D. Bockelée-Morvan, J. Crovisier, T. Encrenaz, M. Küppers, L.-M. Lara, S. Szutowicz, B. Vandenbussche, F. Bensch, E. A. Bergin, F. Billebaud, N. Biver, G. A. Blake, J. A. D. L. Blommaert, J. Cernicharo, L. Decin, P. Encrenaz, H. Feuchtgruber, T. Fulton, T. de Graauw, E. Jehin, M. Kidger, R. Lorente, D. A. Naylor, G. Portyankina, M. Sánchez-Portal, R. Schieder, S. Sidher, N. Thomas, E. Verdugo, C. Waelkens, A. Lorenzani, G. Tofani, E. Natale, J. Pearson, T. Klein, C. Leinz, R. Güsten, and C. Kramer. First results on martian carbon monoxide fromHerschel/HIFI observations. *Astron. & Astrophys.*, 521:L48, 2010a. doi:10.1051/0004-6361/201015159.

P. Hartogh, C. Jarchow, E. Lellouch, M. de Val-Borro, M. Rengel, R. Moreno, A. S. Medvedev, H. Sagawa, B. M. Swinyard, T. Cavalié, and et al. Herschel/HIFI observations of Mars: First detection of o_2 at submillimetre wavelengths and upper limits on HCl and H2O2. *Astron. & Astrophys.*, 521:L49, 2010b. doi:10.1051/0004-6361/201015160.

P. Hartogh, G. R. Sonnemann, M. Grygalashvyly, L. Song, U. Berger, and F.-J. Lï£¡bken. Water vapor measurements at alomar over a solar cycle compared with model calculations by lima. *J. Geophys. Res.*, 115:D00I17, 2010c. doi:10.1029/2009jd012364.

J. L. Hollingsworth and M. A. Kahre. Extratropical cyclones, frontal waves, and Mars dust: Modeling and considerations. *Geophys. Res. Lett.*, 37(22):L22202, 2010. doi:10.1029/2010gl044262.

B. M. Jakosky, R. P. Lin, J. M. Grebowsky, J. G. Luhmann, D. F. Mitchell, G. Beutelschies, T. Priser, M. Acuna, L. Andersson, D. Baird, D. Baker, R. Bartlett, M. Benna, S. Bougher, D. Brain, D. Carson, S. Cauffman, P. Chamberlin, J.-Y. Chaufray, O. Cheatom, J. Clarke, J. Connerney, T. Cravens, D. Curtis, G. Delory, S. Demcak, A. DeWolfe, F. Eparvier, R. Ergun, A. Eriksson, J. Espley, X. Fang, D. Folta, J. Fox, C. Gomez-Rosa, S. Habenicht, J. Halekas, G. Holsclaw, M. Houghton, R. Howard, M. Jarosz, N. Jedrich, M. Johnson, W. Kasprzak, M. Kelley, T. King, M. Lankton, D. Larson, F. Leblanc, F. Lefevre,

R. Lillis, P. Mahaffy, C. Mazelle, W. McClintock, J. McFadden, D. L. Mitchell, F. Montmessin, J. Morrissey, W. Peterson, W. Possel, J.-A. Sauvaud, N. Schneider, W. Sidney, S. Sparacino, A. I. F. Stewart, R. Tolson, D. Toublanc, C. Waters, T. Woods, R. Yelle, and R. Zurek. The Mars Atmosphere and Volatile Evolution (MAVEN) Mission. *Space Science Reviews*, 195(1-4):3–48, 2015. doi:10.1007/s11214-015-0139-x.

R. Kahn. Some observational constraints on the global-scale wind systems of mars. *J. Geophys. Res.*, 88 (A12):10189, 1983. doi:10.1029/ja088ia12p10189.

Y. Kasai, H. Sagawa, T. Kuroda, T. Manabe, S. Ochiai, K. ichi Kikuchi, T. Nishibori, P. Baron, J. Mendrok, P. Hartogh, D. Murtagh, J. Urban, F. von Schéele, and U. Frisk. Overview of the Martian atmospheric submillimetre sounder FIRE. *Planetary and Space Science*, 63-64:62–82, 2012. doi:10.1016/j.pss.2011.10.013.

K. Kikuchi, T. Nishibori, S. Ochiai, H. Ozeki, Y. Irimajiri, K. Y, M. Koike, T. Manabe, K. Mizukoshi, Y. Murayama, T. Nagahama, T. Sano, R. Sato, M. Seta, C. Takahashi, M. Takayanagi, H. Masuko, J. Inatani, M. Suzuki, and M. Shiotani. Overview and early results of the Superconducting Submillimeter-Wave Limb-Emission Sounder (SMILES). *J. Geophys. Res.*, 115:D23306, 2010. doi:10.1029/2010JD014379.

A. Kleinböhl, J. T. Schofield, D. M. Kass, W. A. Abdou, C. R. Backus, B. Sen, J. H. Shirley, W. G. Lawson, M. I. Richardson, F. W. Taylor, N. A. Teanby, and D. J. McCleese. Mars Climate Sounder limb profile retrieval of atmospheric temperature, pressure, and dust and water ice opacity. *J. Geophys. Res.*, 114:E10, 2009. doi:10.1029/2009je003358.

O. Korablev, A. Trokhimovsky, A. V. Grigoriev, A. Shakun, Y. S. Ivanov, B. Moshkin, K. Anufreychik, D. Timonin, I. Dziuban, Y. K. Kalinnikov, and F. Montmessin. Three infrared spectrometers, an atmospheric chemistry suite for the ExoMars 2016 trace gas orbiter. *J. Appl. Remote Sens˙*, 8(1):084983, 2014. doi:10.1117/1.jrs.8.084983.

V. A. Krasnopolsky, G. L. Bjoraker, M. J. Mumma, and D. E. Jennings. High-resolution spectroscopy of mars at 3.7 and 8 μm: A sensitive search for H_2O_2, H_2CO, HCl, and CH_4, and detection of HDO. *Journal of Geophysical Research: Planets*, 102(E3):6525–6534, 1997. doi:10.1029/96je03766.

T. Kuroda and P. Hartogh. Wind velocities of different seasons and dust opacities on mars: comparison between microwave observations and simulations by general circulation models. *Volume 19: Planetary Science(PS)*, pages 261–270, 2010. doi:10.1142/9789812838162_0020.

F. Lefévre, F. Montmessin, N. M. Schneider, J. Deighan, S. K. Jain, A. I. F. Stewart, M. S. Chaffin, M. Crismani, W. E. McClintock, G. M. Holsclaw, B. M. Jakosky, A. Stiepen, D. Y. Lo, R. Yelle, and J. T. Clarke. Mars ozone mapping with MAVEN IUVS. In *Proc. sixth Mars Atmosphere Modeling and Observations conference*, 2017.

E. Lellouch, J. Rosenqvist, J. J. Goldstein, S. W. Bougher, and G. Paubert. First absolute wind measurements in the middle atmosphere of Mars. *Astrophys. J.*, 383:401, 1991. doi:10.1086/170797.

V. Limpasuvan, D. L. Wu, M. J. Schwartz, J. W. Waters, Q. Wu, and T. L. Killeen. The two-day wave in EOS MLS temperature and wind measurements during 2004–2005 winter. *Geophys. Res. Lett.*, 32(17), 2005. doi:10.1029/2005gl023396.

N. J. Livesey and W. G. Read. Direct retrieval of line-of-sight atmospheric structure from limb sounding observations. *Geophys. Res. Lett.*, 27(6):891–894, 2000. doi:10.1029/1999GL010964.

N. J. Livesey, W. V. Snyder, W. G. Read, and P. A. Wagner. Retrieval algorithms for the EOS Microwave Limb Sounder (MLS). *IEEE Trans. Geosci. Remote Sens.*, 44(5):1144–1155, 2006. doi:10.1109/TGRS.2006.872327.

J.-B. Madeleine, F. Forget, E. Millour, T. Navarro, and A. Spiga. The influence of radiatively active water ice clouds on the Martian climate. *Geophys. Res. Lett.*, 39(23), 2012. doi:10.1029/2012gl053564.

M. C. Malin, W. M. Calvin, B. A. Cantor, R. T. Clancy, R. M. Haberle, P. B. James, P. C. Thomas, M. J. Wolff, J. F. Bell, and S. W. Lee. Climate, weather, and north polar observations from the Mars Reconnaissance Orbiter Mars Color Imager. *Icarus*, 194(2):501–512, 2008. doi:10.1016/j.icarus.2007.10.016.

L. Maltagliati, F. Montmessin, A. Fedorova, O. Korablev, F. Forget, and J.-L. Bertaux. Evidence of water vapor in excess of saturation in the atmosphere of Mars. *Science*, 333(6051):1868–1871, 2011. doi:10.1126/science.1207957.

L. Maltagliati, F. Montmessin, O. Korablev, A. Fedorova, F. Forget, A. Määttänen, F. Lefèvre, and J.-L. Bertaux. Annual survey of water vapor vertical distribution and water–aerosol coupling in the martian atmosphere observed by SPICAM/MEx solar occultations. *Icarus*, 223(2):942–962, 2013. doi:10.1016/j.icarus.2012.12.012.

D. J. McCleese, J. T. Schofield, F. W. Taylor, S. B. Calcutt, M. C. Foote, D. M. Kass, C. B. Leovy, D. A. Paige, P. L. Read, and R. W. Zurek. Mars Climate Sounder: an investigation of the thermal and water

vapor structure, dust and condensate distributions in the atmosphere, and energy balance of the polar regions. *J. Geophys. Res.*, 112:E05S06, 2007. doi:10.1029/1006JE002790.

A. S. Medvedev, E. Yiğit, and P. Hartogh. Estimates of gravity wave drag on mars: Indication of a possible lower thermospheric wind reversal. *Icarus*, 211(1):909–912, 2011a. doi:10.1016/j.icarus.2010.10.013.

A. S. Medvedev, E. Yiğit, P. Hartogh, and E. Becker. Influence of gravity waves on the martian atmosphere: General circulation modeling. *J. Geophys. Res.*, 116(E10):E10004, 2011b. doi:10.1029/2011je003848.

A. S. Medvedev, F. González-Galindo, E. Yiğit, A. G. Feofilov, F. Forget, and P. Hartogh. Cooling of the martian thermosphere by CO2radiation and gravity waves: An intercomparison study with two general circulation models. *J. Geophys. Res.*, 120(5):913–927, 2015. doi:10.1002/2015je004802.

I. Mehdi, J. V. Siles, C. Lee, and E. Schlecht. THz diode technology: Status, prospects, and applications. *Proc. IEEE*, 105(6):990–1007, 2017. doi:10.1109/jproc.2017.2650235.

T. I. Michaels, A. Colaprete, and S. C. R. Rafkin. Significant vertical water transport by mountain-induced circulations on Mars. *Geophys. Res. Lett.*, 33(16), 2006. doi:10.1029/2006gl026562.

F. Montmessin, F. Forget, P. Rannou, M. Cabane, and R. M. Haberle. Origin and role of water ice clouds in the Martian water cycle as inferred from a general circulation model. *J. Geophys. Res.*, 109(E10):E10004, 2004. doi:10.1029/2004je002284.

F. Montmessin, O. Korablev, F. Lefèvre, J.-L. Bertaux, A. Fedorova, A. Trokhimovskiy, J. Chaufray, G. Lacombe, A. Reberac, L. Maltagliati, Y. Willame, S. Guslyakova, J.-C. Gérard, A. Stiepen, D. Fussen, N. Mateshvili, A. Määttänen, F. Forget, O. Witasse, F. Leblanc, A. Vandaele, E. Marcq, B. Sandel, B. Gondet, N. Schneider, M. Chaffin, and N. Chapron. SPICAM on Mars Express: A 10 year in-depth survey of the Martian atmosphere. *Icarus*, 297:195–216, 2017. doi:10.1016/j.icarus.2017.06.022.

R. Moreno, E. Lellouch, F. Forget, T. Encrenaz, S. Guilloteau, and E. Millour. Wind measurements in mars' middle atmosphere: IRAM Plateau de Bure interferometric CO observations. *Icarus*, 201(2):549–563, 2009. doi:10.1016/j.icarus.2009.01.027.

P. W. Mote, K. H. Rosenlof, M. E. McIntyre, E. S. Carr, J. R. Holton, J. S. Kinnersley, H. C. Pumphrey, J. M. R. III, J. W. Waters, , and J. C. Gille. An atmospheric tape recorder: The imprint of tropical tropopause temperatures on stratospheric water vapor. *J. Geophys. Res.*, 101:3989–4006, 1996. doi:10.1029/95JD03422.

D. O. Muhleman and R. T. Clancy. Microwave spectroscopy of the mars atmosphere. *Applied Optics*, 34 (27):6067, 1995. doi:10.1364/ao.34.006067.

D. Murtagh, U. Frisk, F. Merino, M. Ridal, A. Jonsson, J. Stegman, G. Witt, P. Eriksson, C. Jimenez, G. Mégie, J. de La Noëë, P. Ricaud, P. Baron, J.-R. Pardo, A. Hauchecorne, E. J. Llewellyn, D. A. Degenstein, R. L. Gattinger, N. D. Lloyd, W. F. J. Evans, I. C. McDade, C. Haley, C. Sioris, C. von Savigny, B. H. Solheim, J. C. McConnell, K. Strong, E. H. Richardson, G. W. Leppelmeier, E. Kyrölä, H. Auvinen, and L. Oikarinen. An overview of the Odin atmospheric mission. *Can. J. Phys.*, 80:309–319, 2002. doi:10.1139/p01-157.

H. Nair, M. Allen, A. D. Anbar, Y. L. Yung, and R. Clancy. A photochemical model of the Martian atmosphere. *Icarus*, 111(1):124–150, 1994. doi:10.1006/icar.1994.1137.

T. Navarro, J.-B. Madeleine, F. Forget, A. Spiga, E. Millour, F. Montmessin, and A. Määttänen. Global climate modeling of the Martian water cycle with improved microphysics and radiatively active water ice clouds. *J. Geophys. Res.*, 119(7):1479–1495, 2014. doi:10.1002/2013je004550.

C. E. Newman, S. R. Lewis, P. L. Read, and F. Forget. Modeling the martian dust cycle, 1. representations of dust transport processes. *J. Geophys. Res.*, 107(E12):6–1–6–18, 2002. doi:10.1029/2002je001910.

D. A. Ortland, W. R. Skinner, P. B. Hays, M. D. Burrage, R. S. Lieberman, A. R. Marshall, and D. A. Gell. Measurements of stratospheric winds by the High Resolution Doppler Imager. *J. Geophys. Res.*, 101(D6): 10351–10363, 1996.

T. Owen, J. P. Maillard, C. de Bergh, and B. L. Lutz. Deuterium on mars: The abundance of HDO and the value of d/h. *Science*, 240(4860):1767–1767, 1988. doi:10.1126/science.240.4860.1767.

H. M. Pickett, R. L. Poynter, E. A. Cohen, M. L. Delitsky, J. C. Pearson, and H. Müller. Submillimeter, millimeter, and microwave spectral line catalog. *J. Quant. Spectrosc. Radiat. Transfer*, 60(5):883–890, 1998. doi:10.1016/s0022-4073(98)00091-0.

D. Priem, F. Rohart, J.-M. Colmont, G. Wlodarczak, and J.-P. Bouanich. Lineshape study of the J=3←2 rotational transition of CO perturbed by N_2 and O_2. *J. Molecular Struct.*, 517-518:435–454, 2000. doi:10.1016/s0022-2860(99)00268-9.

S. Rafkin. The Mars regional atmospheric modeling system: Model description and selected simulations. *Icarus*, 151(2):228–256, 2001. doi:10.1006/icar.2001.6605.

S. C. Rafkin. The potential importance of non-local, deep transport on the energetics, momentum, chemistry, and aerosol distributions in the atmospheres of Earth, Mars, and Titan. *Planetary and Space Science*, 60 (1):147–154, 2012. doi:10.1016/j.pss.2011.07.015.

S. C. R. Rafkin. A positive radiative-dynamic feedback mechanism for the maintenance and growth of Martian dust storms. *Journal of Geophysical Research*, 114(E1), 2009. doi:10.1029/2008je003217.

S. C. R. Rafkin, R. M. Haberle, and T. I. Michaels. The Mars Regional Atmospheric Modeling System: Model description and selected simulations. *Icarus*, 151(2):228–256, 2001. doi:10.1006/icar.2001.6605.

S. C. R. Rafkin, M. R. V. S. Maria, and T. I. Michaels. Simulation of the atmospheric thermal circulation of a martian volcano using a mesoscale numerical model. *Nature*, 419(6908):697–699, 2002. doi:10.1038/nature01114.

W. G. Read, Z. Shippony, M. J. Schwartz, N. J. Livesey, and W. V. Snyder. The clear-sky unpolarized forward model for the EOS Microwave Limb Sounder (MLS). *IEEE Trans. Geosci. Remote Sens.*, 44(5): 1367–1379, 2006. doi:10.1109/TGRS.2006.873233.

S. Robert, A. Vandaele, I. Thomas, Y. Willame, F. Daerden, S. Delanoye, C. Depiesse, R. Drummond, E. Neefs, L. Neary, B. Ristic, J. Mason, J.-J. Lopez-Moreno, J. Rodriguez-Gomez, M. Patel, and G. Bellucci. Expected performances of the NOMAD/ExoMars instrument. *Planetary and Space Science*, 124: 94–104, 2016. doi:10.1016/j.pss.2016.03.003.

C. D. Rodgers. *Inverse Methods for Atmospheric Science, Theory and Practice*. World Scientific, 2000.

L. Rothman, A. Barbe, D. C. Benner, L. Brown, C. Camy-Peyret, M. Carleer, K. Chance, C. Clerbaux, V. Dana, V. Devi, A. Fayt, J.-M. Flaud, R. Gamache, A. Goldman, D. Jacquemart, K. Jucks, W. Lafferty, J.-Y. Mandin, S. Massie, V. Nemtchinov, D. Newnham, A. Perrin, C. Rinsland, J. Schroeder, K. Smith, M. Smith, K. Tang, R. Toth, J. V. Auwera, P. Varanasi, and K. Yoshino. The HITRAN molecular spectroscopic database: edition of 2000 including updates through 2001. *J. Quant. Spectrosc. Radiat. Transfer*, 82(1-4):5–44, 2003. doi:10.1016/s0022-4073(03)00146-8.

H. Savijärvi and T. Siili. The Martian slope winds and the nocturnal PBL jet. *J. Atmos. Sci.*, 50(1):77–88, jan 1993. doi:10.1175/1520-0469(1993)050<0077:tmswat>2.0.co;2.

M. D. Smith. Interannual variability in TES atmospheric observations of Mars during 1999–2003. *Icarus*, 167(1):148–165, 2004. doi:10.1016/j.icarus.2003.09.010.

M. D. Smith, J. C. Pearl, B. J. Conrath, and P. R. Christensen. Thermal emission spectrometer results: Mars atmospheric thermal structure and aerosol distribution. *J. Geophys. Res.*, 106(E10):23,929–23,945, 2001. doi:10.1029/2000je001321.

M. D. Smith, M. J. Wolff, R. T. Clancy, and S. L. Murchie. Compact Reconnaissance Imaging Spectrometer observations of water vapor and carbon monoxide. *J. Geophys. Res.*, 114, 2009. doi:10.1029/2008je003288.

G. Sonnabend, M. Sornig, P. J. Krötz, R. T. Schieder, and K. E. Fast. High spatial resolution mapping of mars mesospheric zonal winds by infrared heterodyne spectroscopy of CO_2. *Geophys. Res. Lett.*, 33(18): n/a–n/a, 2006. doi:10.1029/2006gl026900.

G. Sonnabend, M. Sornig, P. Kroetz, and D. Stupar. Mars mesospheric zonal wind around northern spring equinox from infrared heterodyne observations of CO_2. *Icarus*, 217(1):315–321, 2012. doi:10.1016/j.icarus.2011.11.009.

A. Spiga, J. Faure, J.-B. Madeleine, A. Määttänen, and F. Forget. Rocket dust storms and detached dust layers in the Martian atmosphere. *J. Geophys. Res.*, 118(4):746–767, 2013. doi:10.1002/jgre.20046.

B. M. Swinyard, P. Hartogh, S. Sidher, T. Fulton, E. Lellouch, C. Jarchow, M. J. Griffin, R. Moreno, H. Sagawa, G. Portyankina, and et al. The Herschel-SPIRE submillimetre spectrum of Mars. *Astron. & Astrophys.*, 518:L151, 2010. doi:10.1051/0004-6361/201014717.

A. D. Toigo. A first look at dust lifting and dust storms near the south pole of Mars with a mesoscale model. *J. Geophys. Res.*, 107(E7), 2002. doi:10.1029/2001je001592.

J. Urban, K. Dassas, F. Forget, and P. Ricaud. Retrieval of vertical constituents and temperature profiles from passive submillimeter wave limb observations of the martian atmosphere: a feasibility study. *Applied Optics*, 44(12):2438, 2005. doi:10.1364/ao.44.002438.

P. Varanasi and G. Tejwani. Half-width calculations for CO lines broadened by CO_2. *J. Quant. Spectrosc. Radiat. Transfer*, 11(3):255–261, 1971. doi:10.1016/0022-4073(71)90012-4.

G. L. Villanueva, M. J. Mumma, R. E. Novak, H. U. Kaufl, P. Hartogh, T. Encrenaz, A. Tokunaga, A. Khayat, and M. D. Smith. Strong water isotopic anomalies in the martian atmosphere: Probing current and ancient reservoirs. *Science*, 348(6231):218–221, 2015. doi:10.1126/science.aaa3630.

H. Wang. Martian clouds observed by Mars Global Surveyor Mars Orbiter Camera. *J. Geophys. Res.*, 107 (E10), 2002. doi:10.1029/2001je001815.

J. W. Waters, L. Froidevaux, R. S. Harwood, R. F. Jarnot, H. M. Pickett, W. G. Read, P. H. Siegel, R. E. Cofield, M. J. Filipiak, D. A. Flower, J. R. Holden, G. K. Lau, N. J. Livesey, G. L. Manney, H. C. Pumphrey, M. L. Santee, D. L. Wu, D. T. Cuddy, R. R. Lay, M. S. Loo, V. S. Perun., M. J. Schwartz, P. C. Stek, R. P. Thurstans, K. M. Chandra, M. C. Chavez, G. Chen, M. A. Boyles, B. V. Chudasama, R. Dodge, R. A. Fuller, M. A. Girard, J. H. Jiang, Y. Jiang, B. W. Knosp, R. C. LaBelle, J. C. Lam, K. A. Lee, D. Miller, J. E. Oswald, N. C. Patel, D. M. Pukala, O. Quintero, D. M. Scaff, W. V. Snyder, M. C. Tope, P. A. Wagner, and M. J. Walch. The Earth Observing System Microwave Limb Sounder (EOS MLS) on the Aura satellite. *IEEE Trans. Geosci. Remote Sens.*, 44(5):1075–1092, 2006. doi:10.1109/TGRS.2006.873771.

C. R. Webster, P. R. Mahaffy, G. J. Flesch, P. B. Niles, J. H. Jones, L. A. Leshin, S. K. Atreya, J. C. Stern, L. E. Christensen, T. Owen, H. Franz, R. O. Pepin, and A. S. and. Isotope ratios of H, C, and O in CO_2 and H_2O of the Martian atmosphere. *Science*, 341(6143):260–263, 2013. doi:10.1126/science.1237961.

R. J. Wilson. Evidence for diurnal period Kelvin waves in the Martian atmosphere from Mars Global Surveyor TES data. *Geophys. Res. Lett.*, 27(23):3889–3892, 2000. doi:10.1029/2000gl012028.

D. Wu, M. Schwartz, J. Waters, V. Limpasuvan, Q. Wu, and T. Killeen. Mesospheric Doppler wind measurements from Aura Microwave Limb Sounder. *Adv. Space Res.*, 42:1246–1252, 2008. doi:10.1016/j.asr.2007.06.014.

D. L. Wu and S. D. Eckermann. Global gravity wave variances from Aura MLS: Characteristics and interpretation. *J. Atmos. Sci.*, 65(12):3695–3718, 2008. doi:10.1175/2008jas2489.1.

D. L. Wu and J. W. Waters. Satellite observations of atmospheric variances: A possible indication of gravity waves. *Geophys. Res. Lett.*, 23(24):3631–3634, 1996. doi:10.1029/96gl02907.

Z. J. Ye, M. Segal, and R. A. Pielke. A comparative study of daytime thermally induced upslope flow on mars and earth. *J. Atmos. Sci.*, 47(5):612–628, 1990. doi:10.1175/1520-0469(1990)047<0612:acsodt>2.0.co;2.

R. W. Zurek, J. R. Barnes, R. M. Haberle, J. B. Pollack, J. E. Tillman, and C. B. Leovy. Dynamics of the atmosphere of mars. *Mars*, pages 835–933, 1992.